https://doi.org/10.5194/egusphere-2026-4603
Preprint. Discussion started: 24 August 2026

Tall tower eddy covariance campaign reveals complex emission patterns for carbonyl sulfide

Jesse Soininen[1], Kukka-Maaria Kohonen[2], Stavros Stagakis[3], Ara Cho[4], Betty Molinier[5], Pascal Rubli[6], Rainer Hilland[7], Natascha Kljun[5], and Leena Järvi[1,8]

[1]Institute for Atmospheric and Earth System Research/Physics, University of Helsinki, Helsinki, Finland
[2]Department of Environmental Systems Science, ETH Zurich, Zurich, Switzerland
[3]Department of Environmental Sciences, University of Basel, Basel, Switzerland
[4]Meteorology and Air Quality, Wageningen University & Research, the Netherlands
[5]Department of Earth and Environmental Sciences, Lund University, Sweden
[6]Empa, Swiss Federal Laboratories for Materials Science and Technology, Dübendorf, Switzerland
[7]Environmental Meteorology, Institute of Earth and Environmental Sciences, University of Freiburg, Freiburg, Germany
[8]Helsinki Institute of Sustainability Science, University of Helsinki, Helsinki, Finland

Correspondence: Jesse Soininen (jesse.soininen@helsinki.fi)

Abstract. Carbonyl sulfide (COS) is a useful tracer of gross primary productivity (GPP), but the magnitude and variability of anthropogenic COS emissions in urban environments remain poorly constrained.

COS fluxes were investigated in Zurich, Switzerland, using tall-tower eddy covariance (EC) measurements as part of the ICOS Cities project from August 2022 to April 2023. Source-area variability was analysed using the Flux Footprint Prediction (FFP) model, and compared with biogenic COS fluxes simulated by the Simple Biosphere 4 (SiB4) model.

Zurich acted as a net sink of COS throughout most of the campaign (median -4.4 pmol m^{-2} s^{-1}). The most vegetated south-western sector exhibited approximately three times the COS uptake of the south-eastern sector (-6.7 and -2.1 pmol m^{-2} s^{-1}, respectively), while the south-eastern sector exhibited the weakest uptake, consistent with stronger anthropogenic fluxes. Footprint-weighted land-cover analysis showed that spatial variability in COS exchange reflected the balance between vegetation uptake and anthropogenic fluxes, with the latter masking the biospheric signal in densely built sectors. SiB4 reproduced the seasonal evolution of COS exchange but underestimated the sink following the preceding compound drought event and during an exceptionally warm winter, highlighting limitations in representing stomatal conductance and urban vegetation.

These results demonstrate both the potential and the challenges of using COS as a tracer of urban GPP. Improved anthropogenic COS emission inventories, ecosystem models, and urban flux observations are needed to improve COS-based estimates of urban carbon uptake.

1 Introduction

Around 70 % of the anthropogenic greenhouse gas emissions originate from urban areas (Gurney et al., 2022) where approximately 58 % of the global and 82 % of the Western European population lives (United Nations, 2025). Hence, cities matter a great deal in the efforts to mitigate the effects of and to adapt to climate change. Many cities are working as pioneers to im-

https://doi.org/10.5194/egusphere-2026-4603
Preprint. Discussion started: 24 August 2026

plement their strategies to reach carbon neutrality. However, observation-based validation approaches for any achieved targets still require further development.

Currently, the eddy covariance technique (EC) is the only method for studying ecosystem-scale carbon dioxide (CO_2) exchange directly through observations. It has long been established in agricultural and natural ecosystems and has also proven to be effective in urban areas. However, with a standard EC methodology, only the net ecosystem exchange of CO_2 (NEE) can be measured. Often, this information alone is insufficient for the cities to identify the sectors where the emission reductions would be the most effective. While change in NEE can indicate overall emission trends, NEE alone is not enough to disentangle anthropogenic emission reductions from concurrent changes in biogenic CO_2 fluxes. Thus, there is a tremendous need for a measurement-based partitioning of the urban NEE. Various approaches, including statistical approaches based on air temperature and/or traffic rate (Lee et al., 2021; Kleingeld et al., 2018; Menzer and McFadden, 2017; Song et al., 2013; Matese et al., 2009); footprint models (Stagakis et al., 2019; Crawford and Christen, 2015); and auxiliary measurements (Stagakis et al., 2023; Wu et al., 2022; Salgueiro et al., 2020; Peters and McFadden, 2012; Järvi et al., 2012) have been developed to partition components from NEE. Each of these methods offers distinct advantages, such as improved accuracy for specific applications, while also presenting limitations related to simplifying assumptions, dependence on auxiliary data, or computational cost. In addition, their applicability may be constrained by site characteristics or data availability. These challenges motivate the development of complementary approaches.

Carbonyl sulfide (COS) is the most abundant sulphur-containing gas in the atmosphere with an approximate atmospheric concentration of 400 ppt (Montzka et al., 2007). COS fluxes have been established as a tracer for ecosystem-scale photosynthetic CO_2 uptake, or gross primary production (GPP) (e.g. Asaf et al., 2013; Kohonen et al., 2022). The potential of COS to track CO_2 uptake is based on the similar pathway to the leaf through the leaf stomata. Unlike CO_2, however, COS is not returned to the atmosphere as a part of the plant respiration, but destroyed at the surface of the chloroplast (Wohlfahrt et al., 2012). Thus, if the leaf-related uptake of COS and CO_2 can be parameterised, a GPP estimate can be obtained from COS fluxes (Asaf et al., 2013). In urban areas, this methodology has the potential to help partition the biogenic and anthropogenic components of the measured NEE. The viability of the method has been partly proven in a user-friendly semi-urban environment with a high vegetated cover fraction (Soininen et al., 2025a) but the absence of anthropogenic emissions as a prerequisite for the method (Blonquist et al., 2011) has been shown to not always hold in human-influenced areas (Zanchetta et al., 2023; Estruch et al., 2023; Karl et al., 2020). Recent studies have shown COS sources associated with heat stress in vegetation based on eddy covariance measurements (Thomas et al. , 2026; Commane et al., 2015), gas exchange chamber studies (Sun et al. , 2023), controlled laboratory experiments (Spielmann et al., 2025), and leaf-level measurements demonstrating COS emissions from sunflower leaves (Cho et al., 2026). This may potentially limit applicability of the method during periods of vegetation stress.

Anthropogenic activities are the largest source of atmospheric COS alongside the oceans (Whelan et al., 2018). Zumkehr et al. (2018a) compiled a global inventory of anthropogenic COS emissions from a range of industrial activities, although the individual source estimates remain uncertain. Consequently, the inventory has been shown to have limitations at finer spatial scales: Zanchetta et al. (2023) identified emission sources missing from the inventory, whereas Belviso et al. (2023) reported overestimations of anthropogenic COS emissions in Europe. In urban areas, tire wear has been identified as a potentially

https://doi.org/10.5194/egusphere-2026-4603
Preprint. Discussion started: 24 August 2026

important source of COS emissions (Karl et al., 2020), as elevated temperatures enhance the thermal decomposition of sulfur-containing compounds in tires, releasing COS (Pos and Berresheim, 1993).

This study quantifies the magnitude of urban COS fluxes and explores the spatio-temporal variations of the COS sinks and sources in Zurich, Switzerland. The observed COS fluxes are compared with fluxes modelled by the land surface model Simple Biosphere Model version 4 (SiB4) to identify deviations from the expected biogenic fluxes that may indicate anthropogenic influences in an urban area. The source areas of the observed fluxes are analysed using a flux footprint model to investigate the role of land cover in shaping the measured COS exchange. This work improves the understanding of the opportunities and limitations of using COS as a tracer of GPP in urban environments and provides new constraints on the magnitude and spatial variability of anthropogenic influences on urban COS fluxes.

2 Material and methods

2.1 Site description

Zurich is the largest city of Switzerland with a population of 1.6 million in the metropolitan area and a population density of 4787 inhabitants per km^2 in the urban area. The city is located in the Limmat Valley, which slopes gently towards North-West from Lake Zurich. The valley is bordered by the Albis hills, which rise to 850 meters in the southwest, and a hill range that reaches 600 meters in the northeast. Figure 1 shows the land cover of the city and its immediate surroundings, where the valley-limiting hill ranges are seen as forest areas. The vegetation land cover classes of the map were obtained from the data set by Li et al. (2026), and the other land covers were obtained from a data set by canton of Zurich (Kanton Zürich, 2017). Missing values in the former data set were filled using the latter data set. Of the 12×12 km^2 study area, 35.0 % was covered by trees (deciduous 21.8 %, evergreen 2.9 %, and mixed forest 10.3 %), 33.2 % by lower vegetation (grassland 26.8 % and cropland 6.4 %), 16.2 % by impervious surfaces (paved 8.9 %, roads 4.9 %, other roads 1.1 %, and rail tracks 1.3 %), 9.5 % by buildings (including 0.9 % industrial buildings), and 5.9 % by water. The remaining 0.2 % was covered by soil and rocks or the surface type was unknown. In 2022 there were 747 000 cars in the canton of Zurich, of which 33.8 % were powered by petrol, 20.6 % by electricity, 11.8 % by diesel and 33.8 % were hybrids (Strassenverkehrsamt des Kantons Zürich, 2025). The Swiss railway network was fully electrified already in early 1960's (Moreau, 1960). In terms of primary energy use, land transport accounted for 12.8 % of the total energy demand while air transport, through the combustion of kerosene, accounted for 9.8 % (Stadt Zürich, 2025a). Heat supply of both buildings and industry made up 34.3 % of total energy use, with major contributions from natural gas (14.7 %) and heating oil (8.1 %), complemented by sources like district heating (4.5 %), bio gas (4.2 %) and wood (1.9 %) (Stadt Zürich, 2025a). Electricity was the largest energy carrier (43.1 % of primary energy use; Stadt Zürich, 2025a), more than half of which was obtained via trading (52 %), with the remainder generated from hydropower (21 %), other renewables (2 %), and nuclear power (25 %) (Stadt Zürich, 2025b).

The EC system was installed on a 16.5 m high mast at the top of the Hardau II tower (47.38145° N, 8.51002° E, 111.8 m agl; 520 m asl) located in a residential area in the Western part of the city centre (Figure 1). For this study, four different sectors based on land cover and data availability were examined: North-Eastern (NE; 0°–60°), South-Eastern (SE; 120°–200°), South-

https://doi.org/10.5194/egusphere-2026-4603
Preprint. Discussion started: 24 August 2026

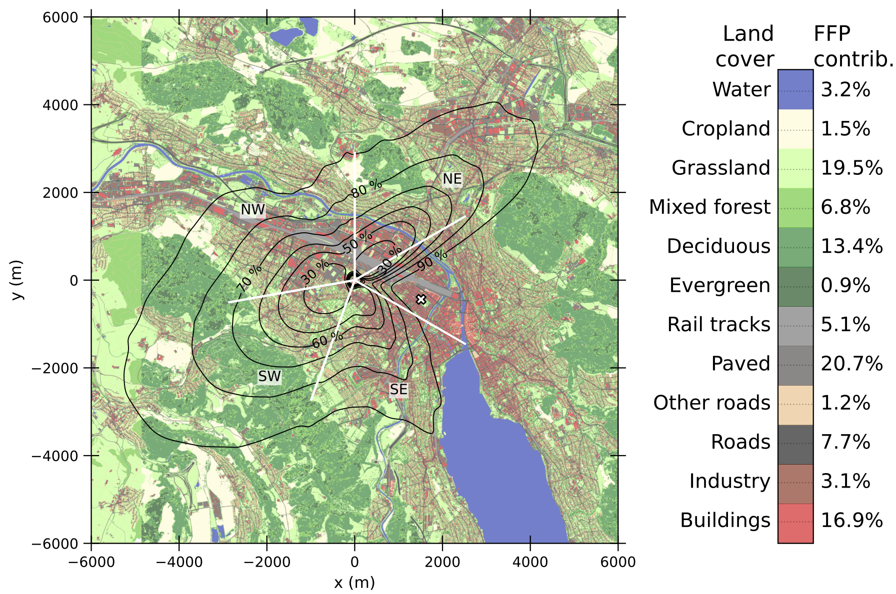

Figure 1. The land cover map around the city of Zurich (Kanton Zürich, 2017). The eddy covariance (EC) system is located at the origin of the map. The percentages denote the contribution of the area to the measured fluxes according to the FFP footprint model (Kljun et al., 2015). The average contribution of each land cover to half-hourly fluxes is indicated in the colour bar label.

Western (SW; 200°–260°), and North-Western (NW; 260°–360°). The 60°–120° sector was excluded because of the orientation of EC setup. To the North is a large railway yard that runs through the city from the East to the North-West of the tower. Even further North are industrial buildings and office spaces up to a distance of 1.5 km before the Limmat river. The South-East area, towards the city centre and the lake, is densely built with residential apartment blocks and is characterized by a higher fraction of surfaces impermeable for water. Directly to the South there is a large cemetery, and to the South-West there is a high fraction of green areas including sports fields, city parks, and private yards. Buildings are mostly residential apartment blocks with open courtyards. In the West there are: a big sport stadium, apartment buildings and some larger industrial buildings.

2.2 EC measurement setup

As a part of the ICOS Cities project (ICOS), an EC measurement campaign of COS was conducted on a tall tower in Zurich, Switzerland. Fluxes of COS, CO_2, CO, and water vapour were measured from 15 August 2022 until 21 April 2023. An ultrasonic anemometer (IRGASON, Campbell Scientific Inc., Logan, UT, US) was mounted together with an unheated inlet tubing of an Aerodyne quantum-cascade laser analyser (AD-QCL; Aerodyne Research Inc, Billerica, MA, USA) 16.5 m above the rooftop. Also, IRGASON measured CO_2 and water vapour but those were not used in the analysis. The IRGASON azimuth angle was 270°. The wind directions from 60 to 120° were excluded from the analysis due to the wake effect of the EC tower, which obstructs and distorts wind measurements in that sector. The tubing lead to an air-conditioned space and consisted of

https://doi.org/10.5194/egusphere-2026-4603
Preprint. Discussion started: 24 August 2026

a 33±2 m long section with an inner diameter of 5.7 mm and a 4 m section with an inner diameter of 4 mm. The latter part had two Acro 50 filters (Pall, Port Washington, NY, USA) to prevent impurities from entering the sample cell of the AD-QCL. Sample air was pumped to the instrument with a constant flow rate of 7.5 l/min using a TriScroll600 pump (Agilent, Santa Clara, CA, USA). A constant pressure of 2.67 kPa (20 Torr) was maintained in the sample cell with an integrated pressure valve. An external cooler was required to operate the AD-QCL, for which a SMC ThermoCon HECR cooling unit (SMC corp., Sotokanda, Chiyoda-ku, Japan) was used.

The IRGASON collected data with 20 Hz frequency, whereas the AD-QCL measured with 10 Hz frequency. To ensure the same temporal resolution and time stamps between datasets, IRGASON data were downsampled to 10 Hz by removing every second anemometer observation after aligning the time stamps with AD-QCL. To minimize drift associated with the AD-QCL instrumentation, a background absorption spectrum was measured with high-purity nitrogen gas (Nitrogen 6.0, Linde, Dagmersellen, Switzerland) and removed from the observed spectra. The background removal was first installed on 17 October 2022, but due to a leak in the system was properly operating only from 8 November 2022 onwards. The sample cell was flushed with nitrogen every four hours for 25 seconds, after which the background spectrum was measured for 10 seconds.

2.3 Auxiliary measurements

Additional meteorological variables from the Kaserne station (47.37759° N, 8.53041° E, 409 m asl) of the Swiss National Air Pollution Monitoring Network (NABEL), located at a courtyard at a distance of about 1.5 km from the Hardau II station were used in this study (Stagakis et al., 2025). An hourly aggregated data set by Stagakis et al. (2024) was used to study the environmental conditions over the measurement period. Kaserne station observations were used because they were considered to be more representative of the ground surface conditions, which the urban vegetation experiences, compared to Hardau II tall tower observations. Important parameters for this work included: air temperature (T_{air}, °C, measurement height 2 m; instrument: HC2A-S3, Rotronic, Bassersdorf, Switzerland), relative humidity (RH, %, 2 m; Thygan VTP 6 OR HC2A-S3), and precipitation (PREC, mm, 2 m; Pluvio^2, OTT Messtechnik, Kampten, Germany). Vapour pressure deficit of air (VPD, kPa, 2 m) was calculated using T_{air} and RH. In addition to Kaserne measurements, soil temperature (T_{soil}, °C, -0.15 m; TEROS 12, Meter group, Pullman, USA) and volumetric soil water content (SWC, m^3 m^{-3}, -0.15 m; TEROS 12) were measured in seven parks in the vicinity of Hardau II (Stagakis et al., 2025, 2024). To frame the temperature conditions of the measurement period, T_{air} data from Kaserne station were obtained for years 2000–2020 from the Swiss National Air Pollution Monitoring Network (Hüglin et al., 2024).

2.4 Eddy covariance flux processing

EC fluxes (F_s^{meas}, mol m^{-2} s^{-1}) were calculated as the covariance between fluctuations in the vertical wind component (w, m s^{-1}) and molar fractions of each relevant substance (χ_s, ppm/ppt). As part of the standard EC raw data processing (Sabbatini et al., 2018; Aubinet et al., 2012), the measured time series were despiked and linearly detrended; a two-dimensional coordinate rotation was subsequently applied. To account for the time lag between instruments, the covariance was maximised within a pre-assigned time window for each 30-min averaging period. For COS, the time lag obtained for CO_2 was used to account for

https://doi.org/10.5194/egusphere-2026-4603
Preprint. Discussion started: 24 August 2026

the low signal to noise ratio of COS measurements (Kohonen et al., 2020). The calculated fluxes were corrected for spectral losses in high frequencies by the instrumentation (Mammarella et al. , 2009) again so that COS correction was taken from CO_2 due to spectral anomaly (see Fig. A1). The anomaly means, in practice, that COS measurement was dominated by noise in high frequencies due to lack of instrumental precision (Gerdel et al. , 2017; Kohonen et al., 2020).

The total flux (F_s^{tot}, mol m^{-2} s^{-1}; Eq. 1) above a homogeneous surface consists of F_s^{meas} and the accumulated concentration under the measurement height, or the storage change flux (F_s^{sto}, mol m^{-2} s^{-1}; Aubinet et al., 2012).

$$F_s^{tot} = F_s^{meas} + F_s^{sto} \tag{1}$$

To assess the storage change flux accurately, a vertical profile of the wanted concentration should be measured as accurately as possible. In the absence of additional measurement points below the EC setup, F_{sto} was estimated by converting the one-point measured molar fraction into true concentration and approximating the vertical rate of change of concentration as in Eq. 2.

$$F_s^{sto} \approx \frac{P}{RT}\frac{\Delta\chi_s(h_{ec})}{\Delta t}h_{ec}. \tag{2}$$

In the equation, P is the atmospheric pressure in Pa at the measurement height, $R = 8.314463$ J K^{-1} mol^{-1} is the universal gas constant, T is the air temperature in K, and h_{ec} is the measurement height in m. Δt indicates the time over which the concentration change at the measurement height ($\Delta\chi_s(h_{ec})$) was observed. The rate of change of molar fraction at the measurement height was estimated using a 5-hour running mean of at least four available data points with 30 minute steps to reduce impact of random noise in the COS measurement by the instrumentation (Kooijmans et al., 2017). To keep the methodology systematic, the same was applied for other gases too. The methodology has been used earlier in more conventional height towers (e.g. Kooijmans et al., 2019; Kohonen et al., 2020) but its suitability for a low concentration trace gas on a tall tower measurement has not been assessed. An additional downside of the methodology is its dependency on accurate molar fraction measurements, which were only available from November onwards. Thus, before November only F_{meas} data are available. Moreover, χ_{COS} had to be additionally filtered because a systematic drift during several background-removal periods was observed. Since (i) the drift could not be corrected in a reproducible way for all periods and (ii) background data are not available for the entire time series, we use the directly measured COS flux, F_{COS}^{meas}, in parts of the analysis instead of the total COS flux, F_{COS}^{tot}.

The flux quality was screened using flux stationarity (FS; Foken and Wichura, 1996) and intermittency (FI; Mahrt et al., 1998), and the individual measurements were quality screened by the kurtosis (Ku) and skewness (Sk) of the half-hourly distribution of observation. A three step flagging system was used, where the best flag (0) was given for periods during which FS< 0.6, FI< 1, $1 <$Ku< 8, and |Sk|< 1. Flag 1 was assigned with criteria FS< 1, |Sk|< 2 and $2 <$Ku< 5. Flag 2 was assigned to all other data, and additionally for missing data. Masking effect of the tower was taken into account by assigning flag 2 when the half-hourly mean wind direction was between 60°–120°. A potential complication for the EC measurements was from a 30 m tall chimney located 150 m to the South-East (140°), which was burning natural gas for residential heating. To account for this, an additional flag 3 was assigned for the times when the chimney was operational, the mean wind direction was between 120–200°, and the flux quality was otherwise assigned a flag of 0 or 1. Chimney operation data were available for 5

https://doi.org/10.5194/egusphere-2026-4603
Preprint. Discussion started: 24 August 2026

minute periods, and the flag was assigned if the chimney emitted during any sub-period within a given half hour. Filtering of the chimney emissions was justified by the interest to urban functions beyond the emissions and, on the other hand, by the chimney plume distorting the actual footprint of the measurements. Table 1 shows the percentages of the different flags separately for F_s^{tot} and F_s^{meas}. The amounts of available storage corrected fluxes were notably lower due to the largely missing credible concentration data. Flux distribution with different quality flags is shown on the Fig. A2. As the distributions of $F_{\mathrm{CO_2}}^{meas}$ and F_{CO}^{meas} were positively skewed (Fig. A2 (d) and (f)), medians are reported throughout the study because they are less sensitive to extreme values than means. Monthly statistics were calculated only for sector-month combinations with at least 30 valid observations.

Table 1. Percentages of the data flags assigned to measured fluxes (F_s^{meas}) and the storage corrected fluxes (F_s^{tot}) during the measurement campaign. Flag 0 indicates the best quality (flux stationarity < 0.6; flux intermittency< 1; $1 <$kurtosis< 8; and $|$skewness$| < 1$), flag 1 is the same but with higher threshold for flux stationarity (1.0). Missing data are assigned flag 2, and flag 3 indicates emissions from a close-by chimney.

Flag	F_{COS}^{meas}	F_{COS}^{tot}	$F_{\mathrm{CO_2}}^{meas}$	$F_{\mathrm{CO_2}}^{tot}$	F_{CO}^{meas}	F_{CO}^{tot}
0	36.3	20.5	39.3	22.1	35.2	20.1
1	14.0	7.7	12.9	7.6	13.9	7.6
2	42.9	66.6	41.8	65.7	44.8	67.7
3	6.7	5.2	6.0	4.6	6.0	4.6

2.5 Footprint analysis

The source areas of the observed fluxes were studied using a FFP footprint model (Kljun et al., 2015) run for Zurich EC tower by Molinier et al. (2026). A footprint is calculated for each 30-min EC flux period, describing the contribution of the area to the measured fluxes represented as a spatial weighting function ($\mathrm{m^{-2}}$) at 10×10 $\mathrm{m^2}$ resolution. The footprints were filtered using the associated boundary layer height flag. To estimate the contribution of different land cover types to the observed fluxes, the footprint estimates were combined with a land cover map aggregated from several datasets covering the municipality of Zurich and its surroundings with 1×1 $\mathrm{m^2}$ resolution (Kanton Zürich, 2017). The land cover map was aggregated to the footprint resolution, and separate fractional cover layers were created for each land cover class. These fractional land cover layers were multiplied element-wise by the footprint weights. The resulting weighted maps were spatially summed for each land cover class and normalized by the sum across all classes to obtain the fractional contribution (p) of each land cover type to each half-hourly flux observation. Mean footprint-weighted contributions of the different land covers, derived from the FFP footprint climatology over the measurement period, are shown in Fig. 1. For each land cover class, both the footprint-weighted contribution and the corresponding areal fraction within a 2.9 km radius were calculated to distinguish the effective contribution to the measured flux from the spatial coverage of the land cover. Radii between 500 m–8.4 km were evaluated, and a radius of 2.9 km was selected because it minimised the mean squared error between the footprint-weighted contributions

https://doi.org/10.5194/egusphere-2026-4603
Preprint. Discussion started: 24 August 2026

and the corresponding areal fractions across all land cover classes in the full-footprint case. Therefore, it was considered the best approximation of the climatological footprint extent.

To study the impact of the land cover and their related activities on the observed fluxes, the correlation between the half-hourly observed fluxes was compared with the simultaneous impact of the FPP-weighted land cover. The datasets were compared by assessing the linear correlation with Pearson's correlation coefficient between each flux and land cover.

$$R_{p,F_s} = \frac{\mathrm{cov}(p, F_s)}{\sigma_p \sigma_{F_s}}. \tag{3}$$

In Eq. 3 the numerator is the covariance between the observed flux F_s and the flux contribution p and the denominator is the product of their standard deviations. Positive correlations indicate higher fluxes originating from the land cover class in question and vice versa.

2.6 SiB4 modelling and flux partitioning

In this study, biogenic COS and CO_2 fluxes were simulated using the land surface model Simple Biosphere Model version 4 (SiB4; Haynes et al. (2019)). SiB4 simulates coupled exchanges of water, energy, and carbon at regional to global scales. Berry et al. (2013) introduced a parameterisation of leaf-level conductances and proposed a COS flux estimation module, which has since been integrated into SiB4, enabling concurrent simulation of CO_2 and COS exchange at the leaf scale.

SiB4 was run at a spatial resolution of 0.5° and a temporal resolution of 3 hours. To ensure equilibrium of carbon and sulphur pools, the model was spun up using five consecutive iterations over the period 2000–2020. The main simulation period covered 2020–2024. For comparison with observations, SiB4 output from the grid cell spanning 47.0–47.5° N and 8.5–9.0° E was extracted, and only the period overlapping with the EC observations (15 August 2022 to 30 April 2023) was used in the analysis.

Atmospheric COS mole fractions used as boundary conditions for SiB4 were derived from optimized COS fields obtained using the TM5 4D-Var inversion framework (Kooijmans et al., 2021). These COS mole fractions were averaged over the period 2016–2018 and provided at a temporal resolution of three hours. More recent global COS boundary condition datasets are not currently available; therefore, the 2016–2018 climatology was used as the best available estimate. A constant atmospheric CO_2 mole fraction of 370 $\mu\mathrm{mol\ mol}^{-1}$ was prescribed. This corresponds to the default atmospheric CO_2 mole fraction used in SiB4 and is lower than the atmospheric CO_2 concentrations during the study period, representing a potential source of uncertainty in the simulations. Meteorological forcing data were obtained from the Modern-Era Retrospective Analysis for Research and Application, version 2 (MERRA-2) reanalysis dataset (Gelaro et al. , 2017).

Plant functional type (PFT) information embedded within SiB4 was used without further modification. The PFT composition of the grid cell covering the study area consisted of C_3 grass (32 %), deciduous broadleaf forest (26 %), evergreen needleleaf forest (14 %), desert and bare ground (12 %), C_3 crops (11 %), and winter wheat (5 %). This composition is broadly consistent with the land cover characteristics of the wider study area, which is dominated by vegetated surfaces and forest. However, the SiB4 grid-cell PFT fractions do not explicitly represent the heterogeneous urban land cover (e.g., impervious surfaces,

https://doi.org/10.5194/egusphere-2026-4603
Preprint. Discussion started: 24 August 2026

buildings, and water bodies) present within the EC footprint. Differences between the model PFT composition and the actual footprint-weighted surface composition may therefore contribute to uncertainty in the simulated fluxes.

Vegetation COS fluxes were simulated following the standard SiB4 framework, with recent updates to parameterisations of COS uptake. The temperature dependence of internal leaf conductance for COS was implemented using the formulation proposed by Cho et al. (2023). In addition, Ball–Woodrow-Berry stomatal conductance parameters for evergreen needle-leaf forest and deciduous broadleaf forest PFTs were updated according to Cho et al. (2023). Soil COS fluxes were calculated using the mechanistic soil model developed by Ogée et al. (2016), as implemented in SiB4 (Kooijmans et al., 2021).

To match the observations with the three-hour temporal resolution of SiB4, observations with quality flags 0 and 1 from the three-hour period were averaged, if at least four observations were available. Measured fluxes were compared with the SiB4 grid-cell flux, calculated as the PFT-fraction-weighted mean of the simulated fluxes. The differences between the observed fluxes and SiB4 modelled fluxes of COS and CO_2 (ΔF_s, mol m^{-2} s^{-1}) were considered as the unidentified component of the flux as in Eq. 4.

$$\Delta F_s = F_s^{meas} - F_s^{\mathrm{SiB4}}. \tag{4}$$

By convention, a sink of substance s is negative. Thus, a positive ΔF_s indicates that either (a) SiB4 overestimates the sink, (b) F_s^{meas} includes additional sources (biogenic or anthropogenic), or (c) the footprint of the half-hourly measurement contains less vegetation (and therefore a smaller expected vegetation sink) than SiB4 model domain. Conversely, a negative ΔF_s indicates that the observed sink is larger than that modelled by SiB4. To avoid biases due to both data gaps and wind directionality, daily mean values were used to calculate ΔF_s. The daily means were calculated only when at least 4 and 10 observations were available for F_s^{meas} and F_s^{SiB4}, respectively, reflecting their different temporal resolutions.

To enable comparison of the magnitude of ΔF_s, independent estimates of both COS and CO_2 anthropogenic emissions (F_s^a, mol m^{-2} s^{-1}) were derived. Values of enhancement factors from earlier research were used. Here, the enhancement factor refers to the ratio of anthropogenic COS and CO_2 enhancements above background concentrations. To estimate F_{COS}^a (pmol m^{-2} s^{-1}), an enhancement factor of COS/CO_2 by Baartman et al. (2022) (0.4 ppt ppm^{-1}) was multiplied with $F_{\mathrm{CO_2}}^{meas}$. They estimated the factor from samples measured at a highway tunnel and, thus, F_{COS}^a from Eq. 5 contains only an estimate of traffic emissions.

$$F_{\mathrm{COS}}^a = 0.4 \frac{\mathrm{ppt}}{\mathrm{ppm}} F_{\mathrm{CO_2}}^{meas}. \tag{5}$$

$F_{\mathrm{CO_2}}^a$ (µmol m^{-2} s^{-1}) was estimated using molar ratios of CO/CO_2 ($\chi_{\mathrm{CO/CO_2}}^{land\ use}$) derived from emission inventories in Zurich (Hilland et al., 2025, Table 4). The molar ratios were provided separately both for the four main sectors (NE, SE, SW, NW) around Hardau II and for road transport and stationary combustion. In this study, it was assumed that the amount of road transport is relative to the flux contribution coming from roads, paved and other roads combined (p_{rt}), and that of stationary combustion relative to the flux contribution of industry and buildings together (p_{sc}). Thus, each half-hourly period had a unique molar ratio from where $F_{\mathrm{CO_2}}^a$ was obtained by multiplying an inverse of the weighted mean of the molar ratios with the CO

https://doi.org/10.5194/egusphere-2026-4603
Preprint. Discussion started: 24 August 2026

flux (Eq. 6).

$$F^{a}_{CO_2} = \left(\frac{p_{sc}\chi^{sc}_{CO/CO_2} + p_{rt}\chi^{rt}_{CO/CO_2}}{p_{sc} + p_{rt}} \right)^{-1} F^{tot}_{CO}. \quad (6)$$

2.7 Global COS emission database

The COS fluxes were compared against a global gridded anthropogenic COS emission database by Zumkehr et al. (2018a). The data set has a resolution of 0.1° × 0.1°, which means that the FFP model domain of Zurich (Fig. 1) covered areas across four grids between 8.4°–8.6° E and 47.3°–47.5° N. For those grids, the available sources in the data set were tire wear, viscose (rayon) production, products of agricultural chemistry, paper and pulp production, and industrial solvents. The sources estimated with equations 5 and 6 were compared with an arithmetic mean of the four available grids. The anthropogenic COS emission estimate for Zurich for the most recent year (2012) available in the data set is shown in Fig. 8 (a).

3 Results

3.1 Environmental conditions

An overview of the daily environmental conditions during the measurement campaign is shown in Fig. 2 and Table A1. Figure 2 (a) displays the observed temperature (T_{air}) compared to the longer term (2000-2020; $\overline{T}_{air}$)) mean temperature. The average temperature was 9.6 °C with the hourly aggregated extremes being -6.0 °C and 30.3 °C on 13 December 2022 and 16 August 2022, respectively. The warmest and longest period above the long-term mean temperature was between 20 December 2022 until 16 January 2023, with a maximum difference of 8.5 °C above average on 1 January 2023. The longest time below the long-term average was observed between 16 September and 1 October 2022 whereas the largest negative difference appeared on the last day of the campaign (-8.4°C on 21 April 2023). 6.1 % of the observed temperatures were below 0 °C. At the time with the lowest measured temperatures the city experienced a short-term snow cover. The temperatures increased up to 19.8 °C in the spring. Vapour pressure deficit (VPD) (Fig. 2 (b)) was on average 0.35 kPa, with maximum being 3.1 kPa coinciding with the highest temperature at the beginning of the measurement period. The measurements were conducted mostly during a relatively humid period with 79.7 % of the observations showing VPD lower than 0.5 kPa.

The measurement period was preceded by a long warm and dry period (Fig. 2 (c)). The hottest and driest weather of the measurement period was recorded already on the second day of the campaign, after which the heaviest hourly rainfall on 17 August 2022 (19.3 mm between 21–22 UTC) started to restore the soil moisture from the minimum SWC of 0.18 m^3 m^{-3} towards the saturated winter values (0.32±0.02 m^3 m^{-3}). The heaviest daily rainfall took place on the 28 September 2022 (33 mm d^{-1}), and the longest period without precipitation was between 6-18 February 2023. The soil temperature (not shown) roughly followed the air temperature, with a minimum temperature of 2.3 °C and a maximum of 27.0 °C.

https://doi.org/10.5194/egusphere-2026-4603
Preprint. Discussion started: 24 August 2026

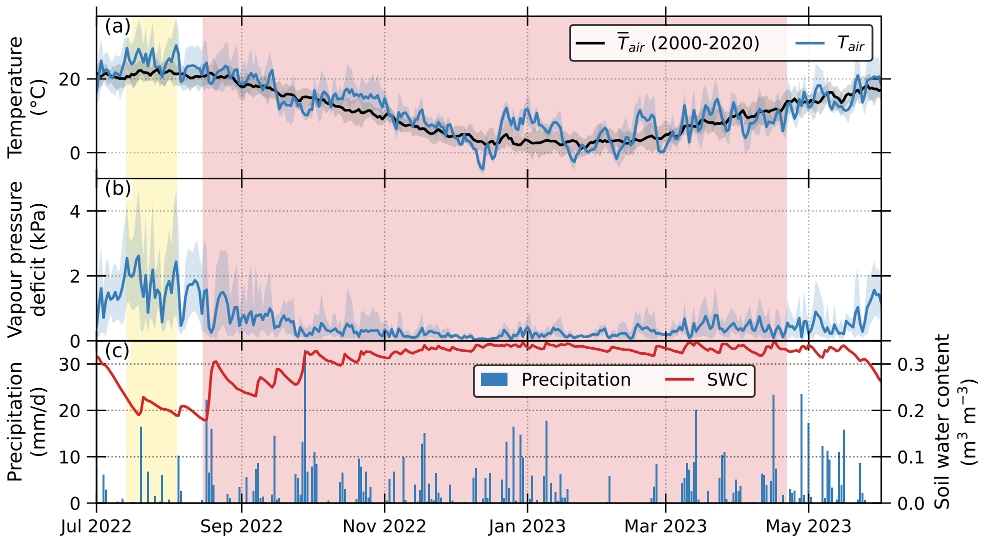

Figure 2. Daily meteorological conditions during the measurement campaign: (a) Air temperature, (b) vapour pressure deficit, and (c) soil water content and precipitation sum. In (a) and (b) the blue line shows the daily mean and the blue shading shows the extreme daily values. In panel (a) a mean temperature and interquartile range (i.e. from 25th percentile to 75th percentile) of the daily observations between years 2000-2020 are shown for comparison with long-term conditions. The yellow shading shows the compound event observed by Scapucci et al. (2024), and the longer, red shading shows the duration of the measurement campaign.

3.2 Diurnal fluxes

Figure 3 shows the diurnal cycles of the measured COS, CO_2, and CO fluxes (flag 0) for each month. Note that August and April are not full months but consist of 16 and 20 full days, respectively. The measured COS fluxes (Fig. 3 (a)) exhibit substantial day-to-day variability, reflected by the wide interquartile ranges, and no clear seasonal evolution is readily apparent from visual inspection. August differs from the other months by exhibiting predominantly positive daytime COS fluxes, whereas the remaining months show fluxes fluctuating around zero with a weak net uptake. The measured CO_2 fluxes (Fig. 3 (b)) show the typical urban diurnal cycle, with the bimodal pattern becoming more pronounced once storage-corrected fluxes are available. The measured CO fluxes remain positive with a pronounced morning peak.

The measured COS and CO_2 fluxes were compared with SiB4 modelling. SiB4 modelled only biogenic fluxes and showed a steady COS sink with a distinguishable diurnal profile over the measurement period (Fig. 3 (a)). The maximum hourly sink of -25.6 pmol m^{-2} s^{-1} was modelled in August. The model estimated the biogenic COS flux to steadily diminish almost completely by mid-December and recover from February onward (Fig. 3). For CO_2 the shape of the diurnal profiles resembled those of COS with an offset due to the modelled respiration (Fig. 3 (b)). The maximum hourly median sink of CO_2 was modelled for August (-6.1 µmol m^{-2} s^{-1}), diminishing towards the end of winter. The biosphere was modelled to be a constant source of CO_2 from November until February, and a net emitter also in October and March.

https://doi.org/10.5194/egusphere-2026-4603
Preprint. Discussion started: 24 August 2026

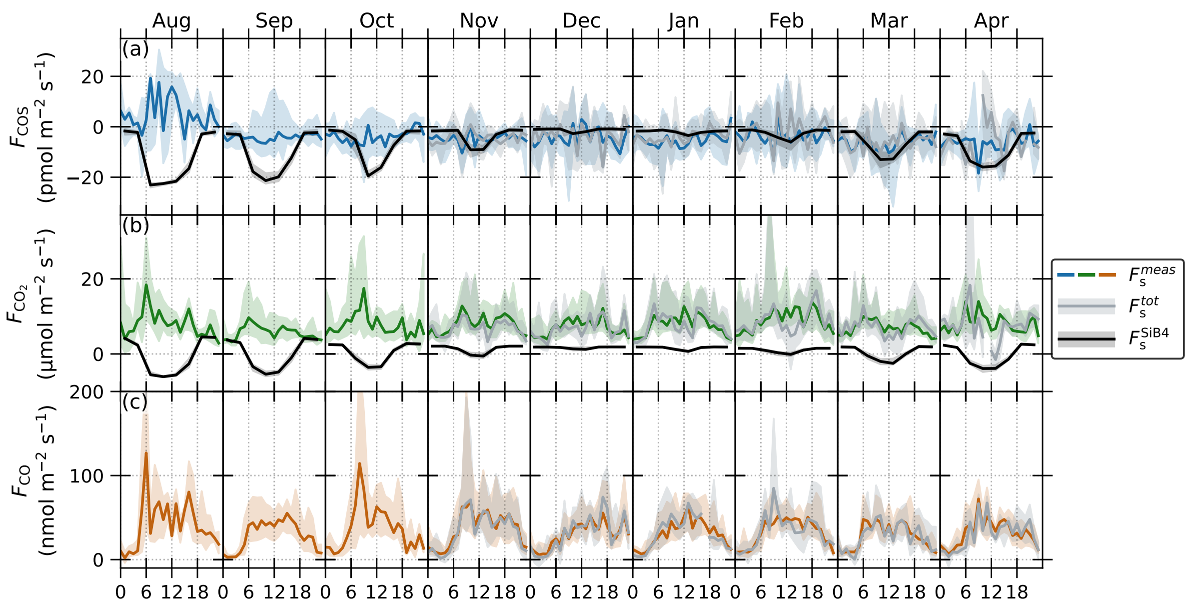

Figure 3. Median diurnal fluxes with the respective interquartile ranges (IQR) for each month and gas. (a) COS, (b) CO_2, and (c) CO. Only quality flag 0 fluxes are shown. The measured fluxes without storage correction are shown with solid coloured lines, storage corrected fluxes with dashed grey lines, and SiB4 modelling with black solid lines. IQR is indicated with the coloured area around the lines. Only hours with at least 5 data points are plotted.

As storage corrections were not available for the whole measurement period, only F_s^{meas} is shown for the times without the correction. Of the estimated storage fluxes, 90 % were found within range -13.6–15.0 pmol m^{-2} s^{-1}, -10.2–9.6 µmol m^{-2} s^{-1}, and -22.0–20.3 nmol m^{-2} s^{-1} for COS, CO_2 and CO, respectively. The relative contribution of the storage flux was, on median, 27 % of the total corrected COS flux and was highest in the afternoon, when the total flux magnitude was close to zero (Fig. A3 (a)). For CO_2, the storage flux accounted for a median of 12 % of the total corrected flux. Storage corrected CO_2 fluxes saw a change to more pronounced two-peaked shape (Fig. A3 (b)). No changes in the flux magnitudes related to the beginning of the nitrogen gas flushing of the sample cell of AD-QCL were observed.

The chimney emitting natural gas combustion products was active fully or partly during 5845 half-hourly periods, of which 807, 718, and 721 coincided with the chosen wind directions (120–200°) as well as good quality (flags 0 and 1) F_{COS}^{meas}, $F_{CO_2}^{meas}$, and F_{CO}^{meas}, respectively. Figure A4 shows the influence of combustion on the fluxes. For $F_{CO_2}^{meas}$ and F_{CO}^{meas} the impact of chimney emissions was most evident at 10 UTC, when the differences to good quality (flags 0 and 1) fluxes were 22.2 µmol m^{-2} s^{-1} and 66.2 nmol m^{-2} s^{-1}, respectively. For F_{COS}^{meas} the maximum difference of 8.4 pmol m^{-2} s^{-1} was observed at 14 UTC.

All the observed monthly median flux values are shown in Table A2. F_{COS}^{meas} showed that the footprint area was a COS sink during 66.6 % of the measurement period with monthly median fluxes ranging from -5.9 to -3.6 pmol m^{-2} s^{-1}. In August, the

https://doi.org/10.5194/egusphere-2026-4603
Preprint. Discussion started: 24 August 2026

fluxes indicated that the footprint area was actually a net source of COS, with a median magnitude of 4.6 pmol m^{-2} s^{-1} with individual hourly median values reaching a maximum of 20 pmol m^{-2} s^{-1} (Fig. 3 (a)). The largest COS sinks were observed in March and April (-5.6 and -5.9 pmol m^{-2} s^{-1}, respectively). The signal was characterised by a relatively constant level and a notable amount of noise with no observable diurnal pattern. The observed CO_2 fluxes showed that the footprint area in Zurich was a near constant source over the whole measurement period (median $F^{meas}_{CO_2}$ 7.1 µmol m^{-2} s^{-1}), with only 3.0 % of $F^{meas}_{CO_2}$ being negative. The months with the storage corrected fluxes showed a shape characteristic for urban areas with peaks in morning and afternoon rush hours. The highest monthly median flux of 9.1 µmol m^{-2} s^{-1} was observed in February and the lowest in September (5.5 µmol m^{-2} s^{-1}). The measured CO fluxes resembled those of CO_2: The footprint area of Hardau II EC setup was a constant emitter of CO (3.6 % of F^{meas}_{CO} negative). The highest monthly median F^{meas}_{CO} were observed in November and February (35 and 34 nmol m^{-2} s^{-1}, respectively) and the lowest in March (24 nmol m^{-2} s^{-1}).

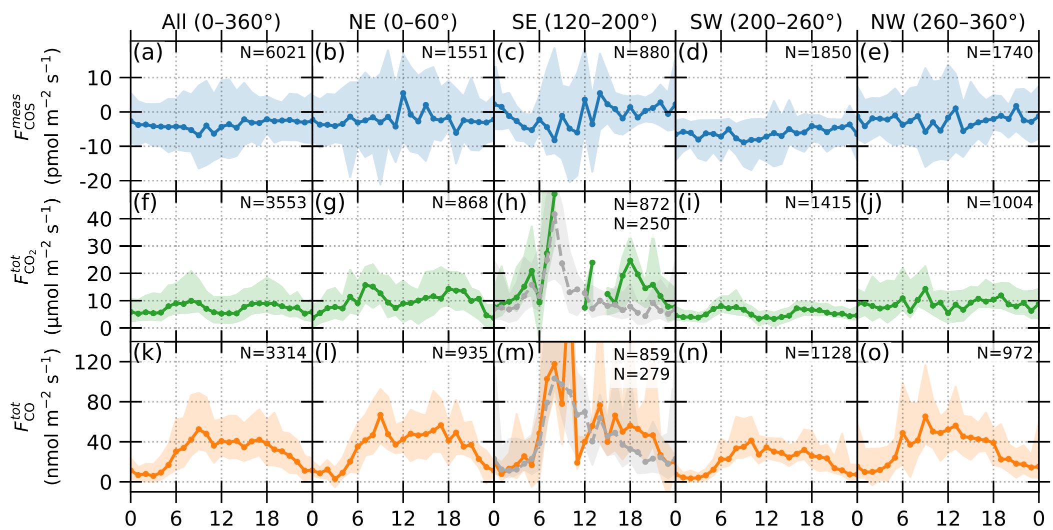

Figure 4. Diurnally observed fluxes separated by wind direction. (a)-(e) F^{meas}_{COS}, (f)-(j) $F^{tot}_{CO_2}$, (k)-(o) F^{tot}_{CO}. Panels (a), (f), and (k) show the full footprint; (b), (g), and (l) North-Eastern sector; (c), (h), and (m) South-Eastern sector; (d), (i), (n) South-Western sector; and (e), (j), and (o) North-Western sector. Only hours with 5 or more observations are shown. As F^{tot}_s had notable gaps for CO_2 and CO in South-Eastern sector, F^{meas}_s were plotted additionally with dashed gray line in panels (h) and (m), where the lower N refers to the number of F^{tot}_s and the higher to the F^{meas}_s. An outlying value in panel (m) has been omitted (see text).

The observed fluxes were dependent on the wind direction, and clear differences were observed between three sectors around Hardau II (see Fig. 4). The SW sector was a sink of COS most of the time (82.5 %) unlike the other sectors (56.9 %, 56.8 % and 60.9 % in SE, SW, and NW, respectively). In Table 2, weighted quantiles are used to account for uneven sampling of wind directions across different temporal scales. F^{meas}_{COS} showed the strongest uptake in the SW sector, which also exhibited the narrowest distribution among the three sectors (IQR: -13.3 to -2.5 pmol m^{-2} s^{-1}). The strongest hourly sink of COS was also observed in the SW sector (-9.6 pmol m^{-2} s^{-1} at 9 UTC), whereas the NE and SE sectors had the strongest COS sources

https://doi.org/10.5194/egusphere-2026-4603
Preprint. Discussion started: 24 August 2026

(5.5 pmol m^{-2} s^{-1} at 12 and 14 UTC, respectively). SE sector had the lowest median sink of COS (-2.1 pmol m^{-2} s^{-1}). $F^{tot}_{\mathrm{CO_2}}$ showed sectoral differences, with lowest median and hourly peak values in SW (5.3 and 8.0 µmol m^{-2} s^{-1}, respectively) and highest in SE (13.5 and 49.0 µmol m^{-2} s^{-1}, respectively). F^{tot}_{CO} fluxes showed lowest median values in the SW sector (18.4 nmol m^{-2} s^{-1}), the SE had the highest medians (45.4 nmol m^{-2} s^{-1}), and the NE and NW sectors had similar values with the medians 32.1 and 33.1 nmol m^{-2} s^{-1}, respectively. Moreover, the peak values were notably higher in the SE sector, where an outlying median peak value of F^{tot}_{CO} (203.6 nmol m^{-2} s^{-1}) was observed at 10 UTC.

Table 2. Medians (and interquartile ranges) of the observed fluxes separated by the wind direction. Values are derived as temporally weighted quantiles to reduce biases associated with uneven sampling of wind directions across the diurnal and seasonal cycles. Only data marked with quality flag 0 were taken into account.

Sector	F^{meas}_{COS} (pmol m^{-2} s^{-1})	$F^{tot}_{\mathrm{CO_2}}$ (μmol m^{-2} s^{-1})	F^{tot}_{CO} (nmol m^{-2} s^{-1})
All (0–360°)	-4.2 (-10.7–4.6)	7.2 (4.0–13.2)	28.2 (10.8–54.3)
NE (0– 60°)	-3.1 (-10.4–8.0)	9.5 (4.1–16.8)	32.1 (13.0–59.1)
SE (120–200°)	-2.1 (-8.6–6.4)	13.5 (8.2–30.7)	45.4 (15.7–88.2)
SW (200–260°)	-6.9 (-13.3—2.5)	5.3 (3.4–7.8)	18.4 (7.9–33.5)
NW (260–360°)	-3.0 (-9.8–5.5)	9.6 (5.5–16.0)	33.1 (14.2–60.7)

The four sectors differed also in their monthly median fluxes (Fig. A5). During most months, SW sector exhibited the most negative F^{meas}_{COS}, reaching -9.4 pmol m^{-2} s^{-1} in April and remaining below other sectors throughout the measurement period. In contrast, NE and NW sectors showed similar seasonal variability with less negative F^{meas}_{COS} than SW sector. The SE sector differed from the others with positive fluxes in September and February, whereas the remaining sectors showed a COS sink during these months. In August, all sectors showed positive F^{meas}_{COS}, except for SW (6.1, 4.3, and 3.2 pmol m^{-2} s^{-1} for SE, NW, and NE, respectively). The median COS flux for the full footprint followed the overall seasonal pattern of the individual sectors, varying from 4.3 pmol m^{-2} s^{-1} in August to between -5.2 pmol m^{-2} s^{-1} and -2.7 pmol m^{-2} s^{-1} during the remaining months. Similar trends apply also for both $F^{tot}_{\mathrm{CO_2}}$ and F^{tot}_{CO}, with the SW sector having the lowest median fluxes during every month and SE sector showing the strongest sources, when there has been enough data to estimate the median.

3.3 Footprints and source area contributions

Based on the FFP, the majority of the flux contribution came from the NE and SW directions with regards to the Hardau II tower (Fig. 1). Approximately 50 % of the flux contribution came fully from the built-up city area, although this estimate should be interpreted with caution because the model does not account for the surrounding valley topography. Estimating from the FFP climatology, the largest contributions to the observed fluxes originated from paved surfaces (20.7 % of the flux contribution), grassland (19.5 %), and buildings (16.9 %). The contributions varied not only with wind direction but also diurnally as the footprint extended further at night-time. The distance from the tower to the peak FFP value varied from the midday minimum of 400 m to the maximum of 600 m at night (Fig. A6). The contribution from land cover classes located mainly further from

https://doi.org/10.5194/egusphere-2026-4603
Preprint. Discussion started: 24 August 2026

the tower, such as deciduous trees, followed the diurnal pattern of the maximum, whereas the contribution from paved surfaces in the city area were inversely proportional to the distance of the FFP maximum.

Table A3 compares the FFP footprint-weighted contributions of different land cover classes with their corresponding area fractions within a 2.9 km radius of the Hardau II tower for the full footprint and each wind sector. In all sectors combined, the largest discrepancy was in the contribution by buildings, which covered 17.7 % of the surface but accounted for 14.4 % of the footprint-weighted contribution. The opposite pattern was observed for rail tracks, which covered 4.1 % of the area but accounted for 6.2 % of the footprint-weighted contribution. After grouping the land cover classes into three categories by summing their contributions (vegetation: grassland, cropland, deciduous, evergreen, and mixed forests; impervious: paved surfaces, roads, rail tracks, and other roads; and built: buildings and industry), a clear sectoral pattern emerged. Vegetated surfaces covered a larger proportion of the study area than their footprint-weighted contribution indicated, whereas built and impervious surfaces contributed disproportionately relative to their areal coverage. The contrast was most pronounced in NE sector, where the footprint-weighted contribution of vegetated surfaces was 24.2 percentage points lower than their areal fraction (31.0 % vs. 54.2 %), whereas the contribution of impervious surfaces was 20.0 percentage points higher (47.2 % vs. 27.2 %). The overrepresentation was driven primarily by rail tracks (15.2 % vs. 4.1 %), paved surfaces (21.6 % vs. 14.2 %), and industry (4.4 % vs. 2.1 %). The SW sector was dominated by vegetated surfaces, which together accounted for 68.5 % of the footprint-weighted contribution. Grassland (30.2 %) and deciduous forest (22.8 %) were the largest individual contributors. Among all sectors, the SW sector also had the lowest contributions from impervious and built surfaces, accounting for 18.3 % and 13.0 % of the footprint-weighted contribution, respectively. The largest contribution of built surfaces was observed in the SE sector (21.1 %, including 1.2 % from industry), whereas the largest contribution of impervious surfaces occurred in the NE sector. Compared with the other sectors, the NW sector showed a more balanced land cover composition, with footprint-weighted contributions broadly reflecting the corresponding areal fractions.

A correlation matrix (Fig. 5) was obtained by analysing the FFP output together with the measured fluxes. Given the heterogeneous nature of the urban footprint, the correlation analysis is interpreted as reflecting relative differences. The correlations were generally weak, consistent with the complexity of the urban footprint, and are therefore interpreted as indicative rather than conclusive. The results were arranged according to the sign and magnitude of the correlations, with positive correlations shown toward the top of the matrix and negative correlations toward the bottom. The vegetated surfaces were associated with lower fluxes and the human-made surfaces and water were associated with higher fluxes. $F^{tot}_{\mathrm{CO_2}}$ had the strongest correlations with the land cover in the flux footprint area. The correlations were strongest, in absolute terms, with grassland (R =-0.34) and roads (R =0.34). For F^{tot}_{CO} the strongest correlation was also found with roads ($R = 0.23$) and deciduous trees (-0.23). F^{tot}_{COS} had a similar but lower correlation with human-made land covers (rail tracks, paved, roads, industry, other roads and buildings; from highest to lowest, all between 0.11–0.13). The strongest negative correlations of COS with grassland and mixed forest (-0.16 and -0.14, respectively) were notably lower than the corresponding values for CO_2 and CO.

Similar analysis of correlation was conducted for four equally long (62 days) sub-periods of the campaign (Fig. A7). The correlations of F^{meas}_{COS} were stronger during the early campaign than during the winter and spring. In terms of absolute values, the highest correlations were found between 15 August – 16 October 2022 and with grassland (R =-0.29), mixed forests

https://doi.org/10.5194/egusphere-2026-4603
Preprint. Discussion started: 24 August 2026

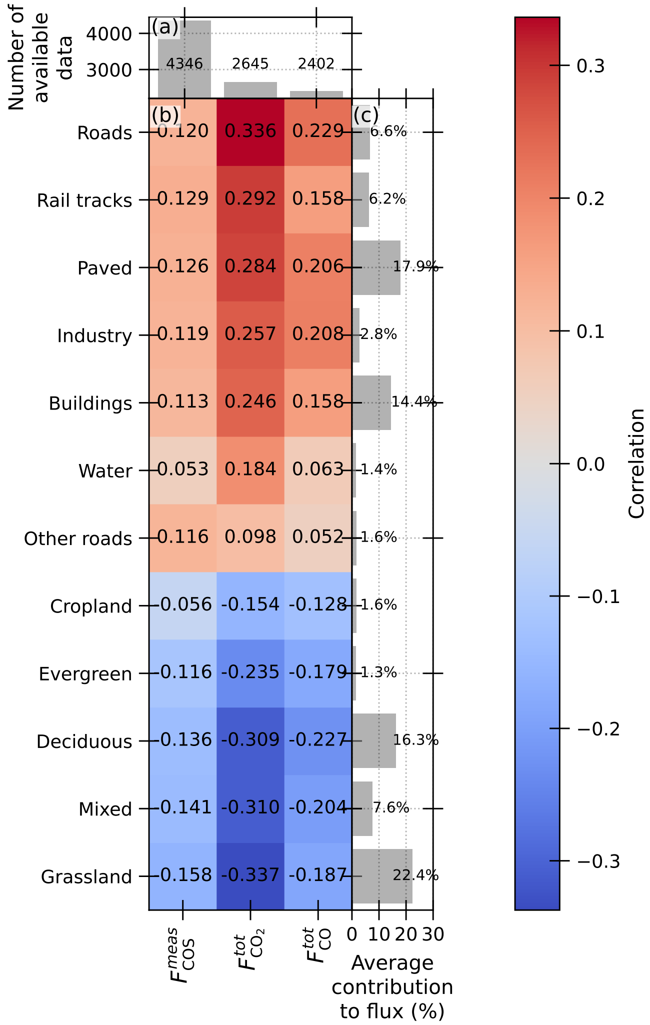

Figure 5. Correlations between the flux contribution from different land covers and fluxes of COS, CO_2, and CO. (a) Available data for each flux, (b) the correlations with their colour bar, and (c) the average contribution of each land cover to the observed fluxes.

(R =-0.24), and paved surfaces (R =0.23). The lowest values were found between 17 October – 18 December 2022, when the correlation with every land cover was between -0.07–0.09, except for buildings (R =0.13) and grassland (R =-0.12). $F^{tot}_{CO_2}$
390 had an increasingly negative correlation with grassland (-0.25 to -0.39) and a constantly positive correlation with human-made surfaces, with a highest R =0.38 with roads between 17 October – 18 December 2022. Correlations between F^{tot}_{CO} and land cover contributions to the flux followed the development of CO_2, only with different surfaces yielding the strongest correlations. The highest correlation was observed with paved surfaces in the autumn (19 December 2022 – 19 February 2023; R =0.41). Overall, positive correlations with human-made surfaces and negative correlations with vegetated land covers
395 prevailed throughout the measurement period for all fluxes.

https://doi.org/10.5194/egusphere-2026-4603
Preprint. Discussion started: 24 August 2026

3.4 SiB4 versus observations

A daily mean difference between SiB4 modelled COS fluxes and the EC observations (ΔF_{COS}) is shown in Fig. 6 together with a daily mean air temperature. From the beginning of the measurement campaign until November the differences were mostly positive. As $F_{\mathrm{COS}}^{\mathrm{SiB4}}$ includes only biogenic fluxes while vegetation and forest covered land covers represent on average 41.7 % of F_{COS}^{meas} contribution, a positive difference is expected during growing period. The difference then became negative, indicating that SiB4 had underestimated the COS sinks during most of the winter until early February after which the values became positive again. There was a cold period in December, during which ΔF_{COS} reached positive values. Afterwards, the values remained negative over the warm period between 20th December 2022 – 16th January 2023. While this is consistent with an underestimation of the COS sink by SiB4, part of the discrepancy may also arise from ecosystem or anthropogenic COS sources and sinks not represented by the model. The extreme values of the daily ΔF_{COS} occurred on 10 February 2023 (52.9 pmol m^{-2} s^{-1}) and 10 March 2023 (-19.0 pmol m^{-2} s^{-1}). The correlation between daily means of ΔF_{COS} and air temperature was 0.41 over the whole measurement period, but varied being 0.64, -0.34, and -0.02 for three equally long sub-periods of the measurement period (15 August – 6 November 2022; 7 November 2022 – 28 January 2023; and 29 January – 21 April 2023, respectively). These differences should be interpreted with caution, as vegetation activity changes substantially over the measurement period. Consequently, the observed correlations may reflect both temperature and seasonal changes in vegetation activity, making it difficult to isolate temperature-related stress effects. Furthermore, the temperature dependency of ΔF_{COS} was different for low and high temperatures: Correlation coefficient was -0.24 for temperatures below 10.0 °C, but 0.68 for temperatures above 13.3 °C (Fig. A8 (a)). The increase in ΔF_{COS} with air temperature suggests that the discrepancy between observations and SiB4 varies with temperature, and is consistent with either an overestimation of COS uptake under warm conditions or the presence of additional temperature-dependent COS sources in the observations. Between the temperatures there was a transition period, where there was no significant correlation to either direction. The difference between measured and modelled CO_2 ($\Delta F_{\mathrm{CO_2}}$) is positive throughout the measurement period, except for an individual day in November (see Fig. A9). As opposed to ΔF_{COS}, there is no clear temperature dependence with $\Delta F_{\mathrm{CO_2}}$ (Fig. A8 (b)).

Sector-separated fluxes of COS and CO_2 are shown in Fig. 7, together with estimates of anthropogenic emissions derived using Eq. 5 and 6 and biogenic fluxes estimated with SiB4 modelling. Both ΔF_{COS} and $\Delta F_{\mathrm{CO_2}}$ showed the lowest median values in the highly vegetated SW sector (Table 3). In this sector, the observed nocturnal sink exceeded that simulated by SiB4, whereas during the daytime the model predicted a stronger sink than was observed. Consequently, ΔF_{COS} was positive only during a short period around noon. In the NW and NE sectors, the model consistently predicted a stronger daytime sink than observed, while the simulated nocturnal fluxes more closely matched the observations. As a result, the median ΔF_{COS} exhibited a pronounced diurnal cycle in all sectors. The NE sector showed a bimodal diurnal pattern, whereas the SE, SW, and NW sectors exhibited a single daytime maximum. The maximum values of the median diurnal ΔF_{COS} were 10.9, 11.9, 3.8, and 12.5 pmol m^{-2} s^{-1} in the NE, SE, SW, and NW sectors, respectively. The estimate of anthropogenic COS emissions (F_{COS}^{a}) showed only a weak diurnal cycle and only momentarily matched ΔF_{COS} around noon in the SW sector. The median F_{COS}^{a} was higher than ΔF_{COS} for the full footprint and all sectors, except for the NW sector.

https://doi.org/10.5194/egusphere-2026-4603
Preprint. Discussion started: 24 August 2026

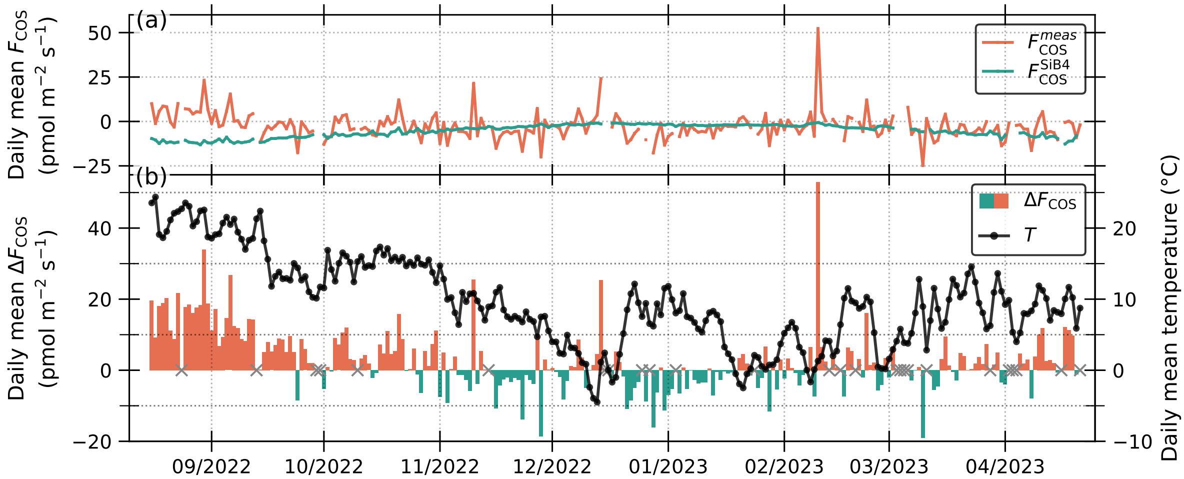

Figure 6. (a) The daily mean observed COS fluxes (F_{COS}^{meas}) and the SiB4 modelled biogenic fluxes ($F_{\mathrm{COS}}^{\mathrm{SiB4}}$). (b) The daily mean difference between F_{COS}^{meas} and $F_{\mathrm{COS}}^{\mathrm{SiB4}}$ (ΔF_{COS}). The difference is indicated with bars: Positive (red) and negative (turquoise) bars indicate that the model has assumed higher or lower sinks of COS compared to measurements, respectively. The days with insufficient amount of data are marked with gray crosses and the black line shows the daily mean temperature.

Table 3. Estimations of anthropogenic fluxes of COS and CO_2 displayed in Fig. 7. Medians (and interquartile ranges) of COS estimates are in pmol m^{-2} s^{-1} and CO_2 in µmol m^{-2} s^{-1}.

Sector	ΔF_{COS}	F^a_{COS}	$\Delta F_{\mathrm{CO_2}}$	$F^a_{\mathrm{CO_2}}$
All	1.9 (-3.6–9.4)	3.3 (2.1–5.1)	7.0 (3.7–11.8)	11.7 (6.4–20.3)
NE	3.2 (-2.7–11.5)	4.4 (2.8–6.1)	10.7 (6.0–15.8)	18.6 (10.0–25.1)
SE	2.8 (-1.8–14.8)	4.3 (2.3–6.6)	13.0 (10.0–27.1)	20.8 (11.8–33.5)
SW	-1.5 (-5.4–3.4)	2.4 (1.8–3.5)	4.5 (2.4–7.0)	7.9 (4.1–12.1)
NW	4.4 (-2.1–12.5)	3.7 (2.3–6.0)	9.5 (5.7–14.4)	18.3 (10.0–24.3)

430 The studied $\Delta F_{\mathrm{CO_2}}$ showed essentially the same pattern as the observed CO_2 fluxes because SiB4 simulated a comparatively low biogenic flux of CO_2. The estimated $F^a_{\mathrm{CO_2}}$ closely matched to the $\Delta F_{\mathrm{CO_2}}$ in all three sectors: At night they matched seemingly well but during the day-time estimated emissions were over twice the magnitude of $\Delta F_{\mathrm{CO_2}}$. The absolute difference is smallest in the SW sector, where the flux magnitudes are overall lower. The medians of $F^a_{\mathrm{CO_2}}$ and $\Delta F_{\mathrm{CO_2}}$ differed most in the NE and NW sectors (7.6 µmol m^{-2} s^{-1}).

https://doi.org/10.5194/egusphere-2026-4603
Preprint. Discussion started: 24 August 2026

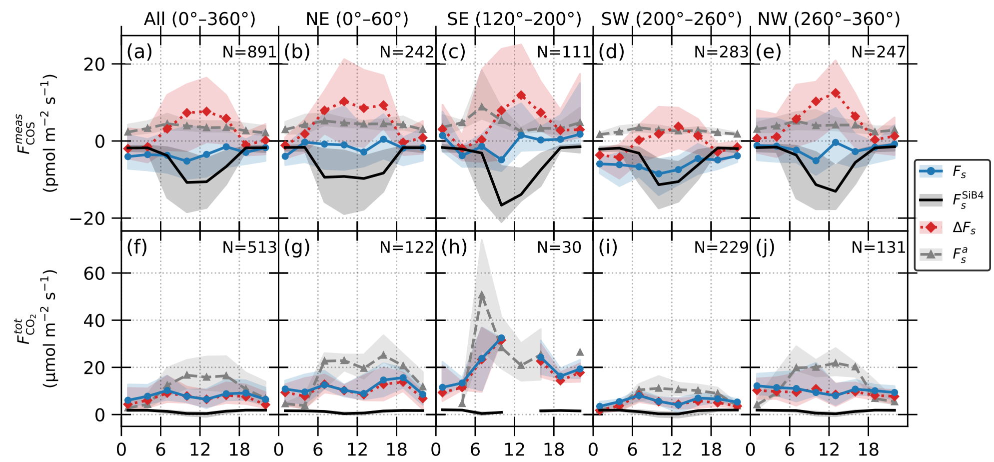

Figure 7. Diurnal partitioned fluxes of (a)-(d) COS and (e)-(h) CO_2. Observed fluxes (F_{COS}^{meas} and $F_{CO_2}^{tot}$) are shown with blue solid lines, SiB4 modelled fluxes (F_{COS}^{SiB4} and $F_{CO_2}^{SiB4}$) with black solid lines, their difference (ΔF_{COS} and ΔF_{CO_2}) with red dotted lines, and estimated anthropogenic fluxes (F_{COS}^{a} and $F_{CO_2}^{a}$) with grey dashed lines. For CO_2 the storage-corrected flux is shown but non-corrected flux is shown for COS. Number of data used (N) for each line is indicated on the plots.

4 Discussion

4.1 Observed flux magnitudes

Despite the nitrogen flush not taking place during the beginning of the measurement period, the fluxes were deemed trustworthy, albeit uncorrected for storage flux. The lack of nitrogen flush did not impact the magnitude of the measured flux, only the availability of the storage correction. As Kohonen et al. (2020) described, the observed negative nocturnal storage flux of COS in (Fig. A3 (a)) indicates a sink in the footprint area during the night hours. In Zurich, however, the storage flux was relatively more important and contributed by median 27 % to the total measured flux, instead of the 19 % maximum contribution reported by Kohonen et al. (2020). The difference is largely explained by the substantially higher measurement height at Hardau II(111.8 m compared with 23 m in Kohonen et al., 2020), which increases the contribution of the storage flux (Montagnani et al., 2018; Lan et al., 2025). In addition, the measured COS fluxes were considerably smaller (median -4.4 versus -11.3 pmol m^{-2} s^{-1} in Kohonen et al., 2020), thereby increasing the relative contribution of the storage flux to the total measured flux. Similar comparison holds with Gerdel et al. (2017), who reported 93 % of all observed storage fluxes to be found between ±2.7 pmol m^{-2} s^{-1} under a measurement height of 2.5 m. As the storage flux is directly proportional with the measurement height (Eq. 2), a higher measurement height–without a profile measurement–leads directly to a larger uncertainty in the total flux, which is notable especially for a low concentration trace gas such as COS.

The observed COS fluxes showed magnitudes similar to the few earlier flux studies that focused on urban environments. The SW sector of Zurich showed a similar daily maximum COS uptake as a street sector in Helsinki (Zue: -9.6 vs. Hel: -

https://doi.org/10.5194/egusphere-2026-4603
Preprint. Discussion started: 24 August 2026

10.6 pmol m^{-2} s^{-1}; Soininen et al., 2025a), with 25 000 cars per day. On the other hand, the diurnal shape of COS fluxes on the more built NE and SE sectors resembled the observations in the city center of Innsbruck during autumn, however, with lower peak sources (Zue: 5.5 vs. Ins: approx. 10–12 pmol m^{-2} s^{-1}; Karl et al., 2020). Also, while Karl et al. (2020) observed a difference between the COS fluxes during weekdays and weekends in Innsbruck, no difference between the workdays and weekends was observed in Zurich. The differences in measured COS fluxes can be, again, explained by the different observational heights. In Zurich, the EC setup was located at 111.8 m above the surface, while in Innsbruck the measurements were made at 42.8 m. Higher elevation will result in longer footprint, which in our case extends beyond the city boundaries into surrounding forested areas that generally act as a sink for COS (Whelan et al., 2018), thereby increasing the influence of non-urban uptake on the observations. The observations in Zurich support the conclusions of earlier studies (Zanchetta et al., 2023; Estruch et al., 2023) that using COS fluxes as a tracer for GPP in human-influenced areas is challenging. This appears to apply also to EC measurements, even in the presence of scattered vegetation, because the assumption of exclusively biogenic COS fluxes is often violated by anthropogenic emissions. As the parks of Zurich are separated from each other by surfaces where COS appears to be emitted from, the required pristine biogenic COS sink is not observed. Over more continuous vegetation cover, on the other hand, COS flux has been shown to be an appropriate proxy for photosynthesis (Soininen et al., 2025a).

The continuous sources of CO_2 were an expected feature from Zurich. The city of Krakow, which is of similar size to Zurich, showed a median winter CO_2 source of 9.4 µmol m^{-2} s^{-1} and a year-round median flux 7.7 µmol m^{-2} s^{-1} from a traffic sector (Jasek-Kamińska et al., 2020), which is close to the Zurich observed median (7.1 µmol m^{-2} s^{-1}). A smaller central European city, Arnhem in the Netherlands, emitted a median of 16.7 µmol m^{-2} s^{-1} year round (Kleingeld et al., 2018). In Arnhem, the smaller footprint area had less vegetated cover than in the full footprint of Zurich, and comparison is closer to the SE sector of Zurich (median 12.5 µmol m^{-2} s^{-1}). The observed CO fluxes from SW sector match the results from a Helsinki street sector (Zue: 18.2 vs. Hel: 23.1 nmol m^{-2} s^{-1} Soininen et al., 2025a). The CO fluxes from NE, SE, and NW sectors (daily median fluxes of 33.2, 33.6, and 33.4 nmol m^{-2} s^{-1}, respectively) were an order of magnitude lower than those observed during winter (347 nmol m^{-2} s^{-1}) and four times lower than those during summer (149 nmol m^{-2} s^{-1}) in Beijing, where residential coal combustion was a major source (Squires et al., 2020). In contrast, the observed fluxes were comparable to the summer-time (June–July) emissions observed in London (39.9 nmol m^{-2} s^{-1}; Helfter et al., 2016).

4.2 Environmental controls on the observed fluxes

As the COS source of the early campaign (August–September) was detected in the NE, SE, and NW sectors rather than being confined to a single wind direction, it appears to have been spatially widespread and therefore more likely driven by environmental conditions than by a specific emission hotspot. Scapucci et al. (2024) reported a compound soil and atmospheric drought event 15 km North-West of Hardau II which ended on 4 August 2022, ten days before the start of the COS flux measurements. As a legacy effect, soil moisture in Zurich was at drought levels at the beginning of the campaign (see Fig 2 (c)), likely contributing to the elevated COS fluxes observed during the first weeks of the measurements.

Previous studies have shown that warm and dry conditions can induce a biogenic COS emissions under controlled conditions (Spielmann et al., 2025) and in disturbed forest ecosystems during prolonged warm and dry periods (Thomas et al. , 2026).

https://doi.org/10.5194/egusphere-2026-4603
Preprint. Discussion started: 24 August 2026

Instead of the vegetation and decomposition of organic matter releasing COS, however, it seems likely that in Zurich it was the preceding compound drought event that decreased the biogenic COS sink of the urban vegetation enough so that the anthropogenic sources momentarily dominated the COS balance. This interpretation is supported by the footprint analysis. During the early campaign, COS sources were observed in the NE, SE, and NW sectors, where vegetated surfaces accounted for 24.8 %, 32.2 %, and 37.1 % of the footprint-weighted contribution, respectively (Table A3). In contrast, the SW sector, where vegetated land covers contributed 60.4 % of the footprint-weighted source area, remained a net COS sink throughout the period. This suggests that the larger vegetated fraction in the SW sector maintained sufficient biospheric uptake despite the preceding drought, whereas uptake in the less vegetated sectors was reduced enough for anthropogenic emissions to contribute more significantly to the net COS exchange. Although drought can also induce soil COS fluxes under low soil water content (SWC) (Maseyk et al., 2014), these fluxes are generally much smaller than vegetation fluxes and are therefore unlikely to explain the observed sectoral differences.

As the measured minimum of soil temperature was above zero, it is assumed that the soil within the footprint area never reached freezing temperatures. Thus, it is further assumed that the soil COS uptake continued throughout the year, except for the aforementioned drought period. Moreover, after October SWC barely decreased below 0.3 m^3 m^{-3}, indicating that the soil did not dry; therefore, the low SWC can be eliminated as the reason for winter-time COS. The SW and NE sectors, which had the highest and lowest flux contributions of vegetation, respectively, showed median COS fluxes of -6.7 and -3.3 pmol m^{-2} s^{-1}. Higher sinks were reported from the Harvard forest in the eastern USA for the dormant period with an unfrozen soil (-7 pmol m^{-2} s^{-1}; Commane et al., 2015) and for an alpine grassland in Austria (-10.3 pmol m^{-2} s^{-1}; Spielmann et al., 2020). On the other hand, a lower winter-time sink varying between -2.4 and -1.5 pmol m^{-2} s^{-1} was measured in a boreal forest stand in Southern Finland (Vesala et al., 2022). In the last case the soil had been frozen and snow-covered, which likely explains the difference to Zurich SW sector observations. The median SE sector sink (-1.9 pmol m^{-2} s^{-1}) was of the same magnitude as the wintry forest uptake, which may reflect both the low vegetation surface fraction and human activities that hide part of the biogenic sink. The COS sink in Zurich could not be attributed between soil, vegetation and other components, unfortunately, but the flat diurnal shape (see Fig. 4) can be taken as an indication of the soil and lower vegetation acting as significant sinks of COS which offset the anthropogenic emissions. At night, the emissions have likely been lower, but same applies to the sinks. The flat shape can also be partially explained by the EC footprint. In the observed fluxes, there was generally a higher contribution of forest sinks during night-time, and an emphasised contribution from the city area during daytime. Thus, the possible human sources would be most visible during the day and weaker in the night-time observations. The impact of other known drivers, such as VPD, were not found as significant drivers of COS uptake during winter.

Using SiB4 to estimate the biogenic COS fluxes was intended to yield an approximation of the order of magnitude of the possible anthropogenic COS emissions, which were expected to be revealed as the difference between the model and the observations. However, a surprising limitation emerged: substantial discrepancies were found between the model and the observations during the exceptional environmental conditions encountered during the campaign. Since these residuals may also reflect anthropogenic emissions, footprint mismatch, and other unrepresented processes, the comparison with SiB4 is most meaningful for the SW sector, where the larger vegetated fraction makes the biogenic contribution dominant. During

https://doi.org/10.5194/egusphere-2026-4603
Preprint. Discussion started: 24 August 2026

both the summer drought and the warm winter period, notable discrepancies between the model and observations remained. In particular, the residual nighttime ΔF_{COS} in the SW sector during winter suggests that SiB4 may underestimate the COS sink under low-radiation conditions. This discrepancy could not readily be explained by factors omitted by the model. Instead, it seems that the low level of radiation forces the uptake to be too small in the model even when the temperature would in reality allow uptake of COS. Similarly, Cho et al. (2023) reported substantial uncertainties in the simulation of stomatal conductance with SiB4 in a boreal forest, which were highlighted at night-time and around winter, resulting in an underestimation of COS sink. During drought conditions, a similar limitation was reported for the previous model version (SiB3), which failed to reproduce a drought-induced biogenic COS source it Harvard forest site (Commane et al., 2015).

In winter, it is likely that a major part of the COS sink originated from the soil, which remained a sink after being rewetted by the autumn rains. However, uptake by low vegetation and coniferous trees cannot be ruled out. Stagakis et al. (2025) simulated the CO_2 exchange in green areas of Zurich using three ecosystem models and found an increase in GPP during winter, although it was outweighed by the increase in ecosystem respiration due to elevated temperatures. Still, if vegetation productivity indeed increased during winter, a corresponding uptake of COS would also be expected. An estimate of GPP independent of land surface models could therefore provide additional insights to the functioning of the urban vegetation.

4.3 Partitioning of biogenic and anthropogenic fluxes

The measurement campaign revealed distinct spatial patterns in COS exchange that reflected differences in both anthropogenic activity and vegetation cover. In August, during the first weeks of the campaign, the NE, SE, and NW sectors acted as sources of COS, whereas the SW sector remained a sink (Fig. A5). The strongest positive fluxes originated from the SE sector (6.1 pmol m^{-2} s^{-1}), where roads, buildings, and paved surfaces together accounted for over 54 % of the footprint-weighted contribution. Conversely, vegetated surfaces were associated with the lowest COS fluxes, suggesting that increasing vegetation contribution promoted biogenic COS uptake. Notably, the NW sector, despite having the highest footprint-weighted vegetation contribution among the source sectors (43.9 %), remained a net source of COS, whereas the SW sector, with a substantially higher vegetation contribution (68.5 %), acted as a sink.

The correlation analysis further showed that rail-track-covered areas were associated with more positive fluxes. However, there is no evidence that the railways themselves emitted COS, as trains in Switzerland have been powered exclusively by electricity for decades (Moreau, 1960). Instead, the 15.2 % footprint contribution of rail tracks in the NE sector likely reflects nearby anthropogenic sources that are indistinguishable from the railway in the land cover analysis.

As the effects of the preceding drought event (Stagakis et al., 2025; Scapucci et al., 2024) subsided in late August–September 2022 (Fig. 2 (c)), vegetation was also expected to begin transitioning towards autumn dormancy. Consequently, biogenic COS uptake was expected to decline, making anthropogenic emissions more apparent. Instead, the observed COS sources diminished. The SW sector remained the least affected owing to its highest footprint-weighted contribution of vegetation as well as the larger, more contiguous green areas compared to other sectors. More fragmented green areas are generally more exposed to edge effects, including elevated temperatures and reduced soil moisture (Garvey et al., 2022), which may increase vegetation stress during drought. It is therefore possible that vegetation in the NE, SE, and NW sectors was more vulnerable to drought

https://doi.org/10.5194/egusphere-2026-4603
Preprint. Discussion started: 24 August 2026

than vegetation in the SW sector, resulting in a greater reduction in COS uptake and consequently altering the balance between biogenic uptake and anthropogenic emissions. This interpretation is further supported by the spring observations, during which all sectors acted as net sinks of COS, indicating that once vegetation recovered from drought and resumed active growth, biogenic uptake was sufficient to dominate the sectoral COS exchange despite differences in surrounding anthropogenic land use.

Subtracting the SiB4 fluxes from the observed fluxes provided an estimate of the residual flux, ΔF_s, which was assumed to be predominantly anthropogenic despite the limitations discussed above. For COS, the differences were substantial. Whereas the modelled fluxes exhibited a pronounced diurnal cycle that was absent from the observations, the resulting subtraction yielded ΔF_{COS} with an inverse diurnal pattern, showing the highest apparent emissions around midday and comparatively low fluxes during the night. In the SW sector, where the observed COS uptake persisted throughout the night, the subtraction yielded an apparent non-biogenic sink. This is likely an artefact arising from an underestimation of the biogenic COS sink by SiB4, reflecting limitations in the representation of residual stomatal conductance. On the other sectors, the agreement between the modelled and observed nocturnal COS sink was considerably better than in the SW sector, suggesting that the largest model deficiencies were confined to the SW sector.

The estimated anthropogenic COS emissions (F^a_{COS}) based on CO_2 co-emission from road traffic did not fully explain the observed ΔF_{COS}. The largest discrepancies occurred during night-time, when the simple co-emission model overestimated COS emissions by assuming that the anthropogenic COS source could be represented solely through co-emissions with traffic-related CO_2 and followed a constant diurnal profile. In reality, traffic intensity decreases substantially during the night, whereas the model attributes the full co-emission to the traffic sector throughout the day. Consequently, the estimated nocturnal COS source remained larger than expected. Furthermore, in the SW sector, where roads accounted for only 5.0 % of the footprint-weighted contribution (Table A3), the estimated traffic-related COS emissions aligned only weakly with the observed daytime peak. The daytime peaks of ΔF_{COS} in the NE, SE, and NW sectors reached 10.9, 11.9, and 12.5 pmol m^{-2} s^{-1}, respectively, closely matching the autumn COS fluxes observed in Innsbruck, where daytime maxima reached approximately 10–12 pmol m^{-2} s^{-1} (Karl et al., 2020).

The estimated anthropogenic COS and CO_2 fluxes indicate that the observed co-occurrence of both gases was related to human activities. The poorest agreement in the SW sector suggests that the assumption of anthropogenic co-emission is insufficient where natural processes dominate the exchange, as wintertime COS uptake and CO_2 release by vegetation weaken the relationship between the two gases. For COS, the discrepancy between the estimated anthropogenic emissions and ΔF_{COS} further highlights the limitations of representing urban COS emissions solely through CO_2 co-emissions. The estimated levels of anthropogenic emissions and their difference from the observed fluxes indicate that the measurements were, to a large extent, influenced by the surrounding ecosystems rather than representing the urban area of Zurich alone.

For CO_2, only minor differences were found between the estimated anthropogenic fluxes and ΔF_{CO_2}, reflecting the dominance of anthropogenic emissions over the comparatively weak biogenic exchange during winter. Consequently, the residual CO_2 flux closely represented the anthropogenic contribution in all sectors.

https://doi.org/10.5194/egusphere-2026-4603
Preprint. Discussion started: 24 August 2026

Overall, the residual flux approach demonstrated that COS and CO_2 behaved fundamentally differently in the urban environment. During the dormant season, anthropogenic CO_2 emissions dominated the observed exchange, and ΔF_{CO_2} therefore provided a robust estimate of the anthropogenic contribution. In contrast, the interpretation of ΔF_{COS} remained strongly dependent on the representation of biogenic uptake. Nevertheless, the daytime maxima of ΔF_{COS} in the NE, SE, and NW sectors closely matched the autumn COS fluxes observed in Innsbruck (Karl et al., 2020), suggesting that the estimated residual fluxes were of a realistic magnitude. The remaining discrepancies, particularly in the SW sector, suggest that residual stomatal uptake of COS during the dormant season is underestimated by current biogenic models. Together, these results demonstrate that urban COS exchange reflected a combination of anthropogenic emissions and biogenic uptake, with the latter exerting a stronger influence on the measured fluxes than expected even during the dormant season.

4.4 Comparison with global COS budget

The anthropogenic COS emissions predicted by the global inventory for the grid cells surrounding the eddy covariance sites in Zurich, Helsinki, and Innsbruck are shown in Fig. 8. For Zurich, the four surrounding grid cells contain emission estimates ranging from 31.1 to 70.1 pmol m^{-2} s^{-1}, with a mean of 45.1 pmol m^{-2} s^{-1}. Even the lowest inventory estimate exceeded the largest daytime values of ΔF_{COS} observed in this study (12.5 pmol m^{-2} s^{-1}), suggesting that the inventory substantially overestimates anthropogenic COS emissions in the Zurich region. For the Zurich grid cells, the inventory attributes 62 % of the anthropogenic COS emissions to tire wear, 27 % to rayon staple or viscose production, and 10 % to rayon yarn production, with the remaining fraction arising from agricultural chemical use, pulp and paper production, and industrial solvent use. Although Zurich has historically played an important role in the silk and viscose industry and was associated with the development of the viscose process (Kauffman, 1984), there is no evidence of present-day manufacturing that could account for nearly one quarter of the estimated emissions. In the global inventory, national viscose production was downscaled using N_2O emissions as a spatial proxy because N_2O is also emitted during viscose production (Zumkehr et al., 2018a). The comparison with the Zurich observations suggests that this approach substantially overestimates COS emissions in the study area. A similar limitation was identified by Belviso et al. (2023), who showed that the N_2O-based downscaling considerably overestimated anthropogenic COS emissions in the Paris region while underestimating emissions from French industrial sources associated with viscose-related production.

According to the global inventory, tire wear contributes between 18.2 and 44.2 pmol m^{-2} s^{-1} to the anthropogenic COS emissions in the four Zurich grid cells. However, even the largest daytime values of ΔF_{COS} observed in this study (10.9–12.5 pmol m^{-2} s^{-1}) remained well below this range. Laboratory experiments have shown that COS emissions from tire rubber increase strongly with temperature (Pos and Berresheim, 1993). Consequently, if tire wear were the dominant anthropogenic COS source in Zurich, its influence would be expected to be particularly apparent during the warm and dry conditions encountered during the early autumn measurements. No evidence for such a large tire-wear source was found. At the Helsinki site, where the global inventory attributes 2.9–39.8 pmol m^{-2} s^{-1} of anthropogenic COS emissions to tire wear, COS uptake was nevertheless observed even in the street sector during summer, where road traffic dominated the anthropogenic emissions (Soininen et al., 2025a). Rather than an enhanced COS source, the observed fluxes remained a net sink throughout the mea-

https://doi.org/10.5194/egusphere-2026-4603
Preprint. Discussion started: 24 August 2026

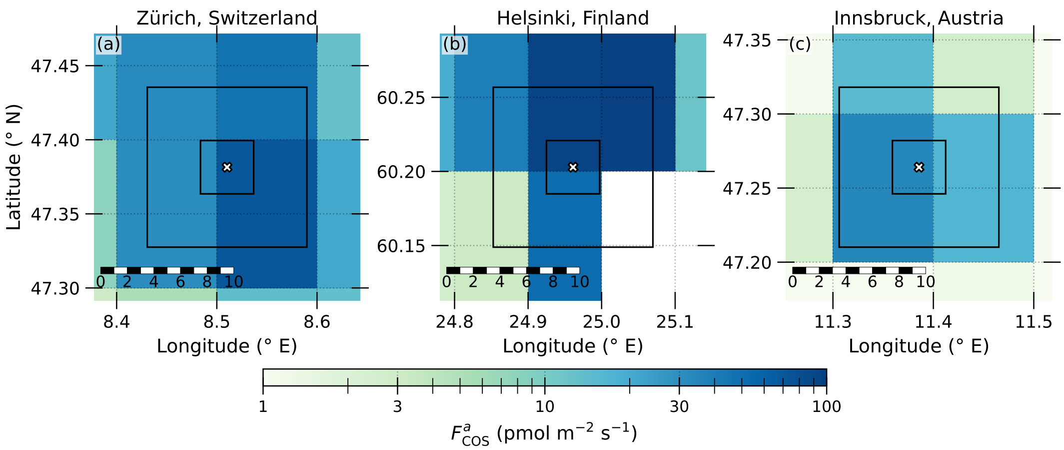

Figure 8. Total anthropogenic COS emissions for 2012 extracted from the global dataset of Zumkehr et al. (2018a) for the inventory grid cells surrounding the eddy covariance towers in (a) Zurich, (b) Helsinki, and (c) Innsbruck. Each panel covers an area of 20 × 20 km. The outer (12 × 12 km) and inner (4 × 4 km) boxes provide a common spatial reference centred on each tower, illustrating the scale of the local surroundings relative to the inventory grid resolution.

surement period. Together with the Zurich observations, this suggests that tire wear contributes less to urban COS emissions than assumed in the global inventory.

Most importantly, natural gas combustion is not represented in the global anthropogenic COS inventory of Zumkehr et al. (2018a). This omission may contribute to discrepancies when applying the inventory to European cities, where natural gas commonly represents an important source of heat production. In Zurich, for example, natural gas accounts for 14.7 % of the total primary energy demand (Stadt Zürich, 2025a). By contrast, the omission of coal combustion from the Swiss inventory is unlikely to substantially affect the comparison, as coal is no longer used to any significant extent for energy production in Zurich (Stadt Zürich, 2024). Similarly, emissions from pigment production, identified by Zumkehr et al. (2018a) as one of the major global anthropogenic COS sources, are not included in the inventory for Switzerland.

4.5 Uncertainty and limitations of the used methodologies

The measurement setup in Hardau II had also some uncertainties. Firstly, COS is a trace gas with low concentration and is thus difficult to measure precisely. This can particularly affect the uncertainty of EC measurements at high measurement levels as at the Hardau tower. In hindsight, it became apparent that the four hourly nitrogen flush is not enough to keep the performance of AD-QCL stable for COS measurements. Consequently, the fraction of data for which storage-corrected fluxes could be calculated decreased from 39.4 % to 16.8 %.

On a diurnal scale, the footprints extended the furthest during night-time under the most stable boundary-layer conditions. During the day, on the contrary, the fluxes came mostly (80 % contribution, not shown) from the closest 3 km radius of the tower. Thus, a significant part of the nocturnal fluxes was not describing the activity in the urban area, but rather the surrounding

https://doi.org/10.5194/egusphere-2026-4603
Preprint. Discussion started: 24 August 2026

forested areas. The impact of advection on the measured signal was neglected, but it may be significant (Jocher et al., 2018), particularly during stable and calm conditions, which can lead to decoupling between the surface and the measurement height (Lan et al., 2025). Consequently, a tall tower EC measurement without a profile measurement for the storage flux estimation often has a high uncertainty (Finnigan , 2006). Keeping in mind the difficulties of operation and the tricky landscape, similar campaigns in the future should be carefully considered.

FFP modelling (Kljun et al., 2015) together with the land cover map proved to be a useful tool when interpreting the fluxes, but it also has limitations. In urban environments, footprint models are subject to uncertainties arising from the heterogeneous roughness length, complex building morphology, and the influence of the urban canopy layer, all of which can affect the estimated source area. Consequently, the calculated footprints should be interpreted as approximations of the contributing surface rather than exact representations. Estimating flux footprints in urban environments using analytical models is inherently challenging because of the complex surface structure (Auvinen et al., 2017). Moreover, measurements from a single EC tower are inherently weighted towards the surfaces located closest to the tower, while contributions from more distant parts of the city are progressively weaker. Thus, the observations from a single EC tower cannot be regarded as representative of the entire urban area (Molinier et al., 2026), but rather of the footprint-weighted source area under the prevailing meteorological conditions. This weighting also results in overlap between land-cover classes, such that the estimated contribution of an individual surface type reflects the mixed composition of the footprint rather than fluxes originating exclusively from that surface.

The SiB4 model is one of the most used ecosystem models of COS fluxes. The model was used to provide a baseline estimate of the biogenic COS fluxes so that any anthropogenic emissions could be identified from the measured signal through a simple subtraction in the Zurich urban environment, where anthropogenic emissions and biospheric fluxes are expected to be the dominant contributors to the observed COS fluxes. However, the comparison with the measurements showed that the model was not able to capture special conditions including winter drought and heatwave conditions. Partly this was due to the MERRA-2 reanalysis not perfectly capturing the conditions affecting the smaller scale features of the EC footprint area. Using local meteorological observations might have led to different results but MERRA-2 was chosen as it is more accurate for larger model domain of SiB4. The model underestimated the sink during winter, when neither the vegetation nor the soils were assumed to have significant contributions to the measurements. This discrepancy may partly reflect the difficulty of representing residual stomatal conductance in land surface models (Cho et al., 2023). Still, it came as a surprise that the modelled sink of COS was actually smaller than the one measured at the tall tower. Several factors may explain this discrepancy. The spatial resolution of SiB4 (0.5°x0.5°) was much coarser than the study area, meaning that the prescribed plant functional types may not have adequately represented of the urban vegetation or the vegetation located on the nearby hills.

5 Conclusions

In this study, a tall-tower eddy covariance measurement campaign was conducted in Zurich, Switzerland, from August 2022 to April 2023 to investigate COS fluxes together with CO_2 and CO. The aim was to quantify the magnitude and variability of COS exchange in a densely built urban environment and to evaluate the potential of COS as a tracer of urban gross primary

https://doi.org/10.5194/egusphere-2026-4603
Preprint. Discussion started: 24 August 2026

production. The measured COS fluxes were analysed together with FFP flux footprint modelling (Kljun et al., 2015) and simulations of biogenic COS exchange using the SiB4 model.

The footprint-weighted urban area acted as a net COS sink for most of the measurement period (66.6 % of the observations; median flux -4.4 pmol m^{-2} s^{-1}), despite persistent anthropogenic emissions. Considerable spatial and temporal variability was observed, with the strongest sources associated with sectors dominated by impervious surfaces, while the most vegetated sector remained a net sink throughout the campaign. Comparison with footprint-weighted land-cover composition demonstrated that vegetation was the dominant control of the observed COS uptake, whereas anthropogenic emissions increasingly masked the biospheric signal in more densely built areas.

The SiB4 model reproduced the general seasonal evolution of the biospheric COS flux but failed to capture several observed features, including the reduced uptake following the preceding compound drought event and the unexpectedly large wintertime sink. The discrepancies likely arose from a combination of factors, most notably limitations in the representation of stomatal conductance (Cho et al., 2023), together with the coarse model resolution and the use of reanalysis meteorological forcing, which cannot fully represent the environmental conditions within the urban footprint.

Overall, the results demonstrate both the potential and the challenges of using COS as a tracer of urban GPP. Anthropogenic emissions were generally lower than predicted by the widely used global inventory but were sufficiently large to complicate the interpretation of urban COS fluxes. The study highlights the need for improved anthropogenic COS emission inventories, continued long-term flux observations, and ecosystem models capable of representing urban vegetation and environmental stress, all of which are essential for improving COS-based estimates of urban carbon uptake.

Appendix A: Supplementary data

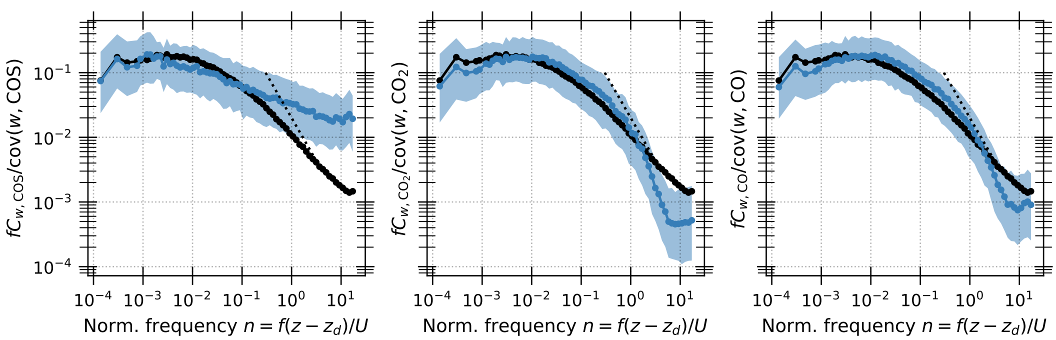

Figure A1. The co-spectra of T and (a) COS, (b) CO_2, and (c) CO and the vertical wind speed. Black line denotes the median co-spectrum of w and T, coloured line is the median co-spectrum of each gas and w and the coloured area denotes the interquartile range (25th to 75th percentile). Dotted line denotes the theoretical slope of -4/3. Both axes have logarithmic scales.

https://doi.org/10.5194/egusphere-2026-4603
Preprint. Discussion started: 24 August 2026

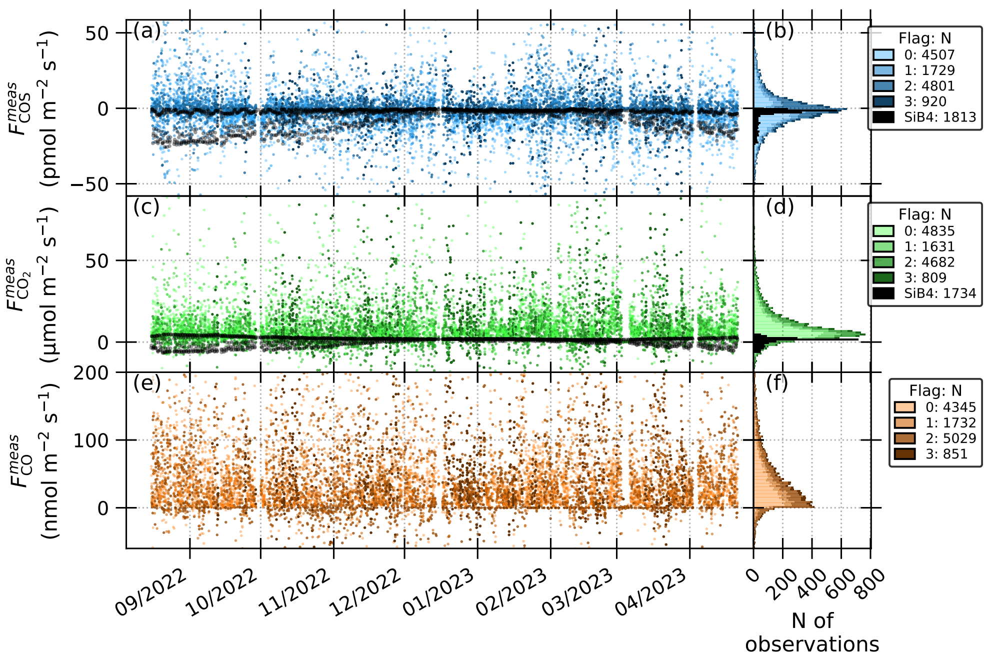

Figure A2. The observed fluxes and the distributions of the quality flags of (a)-(b) COS, (c)-(d) CO_2, and (e)-(f) CO in Hardau II tower in Zürich, Switzerland, between 15 August 2022 and 21 April 2023.

https://doi.org/10.5194/egusphere-2026-4603
Preprint. Discussion started: 24 August 2026

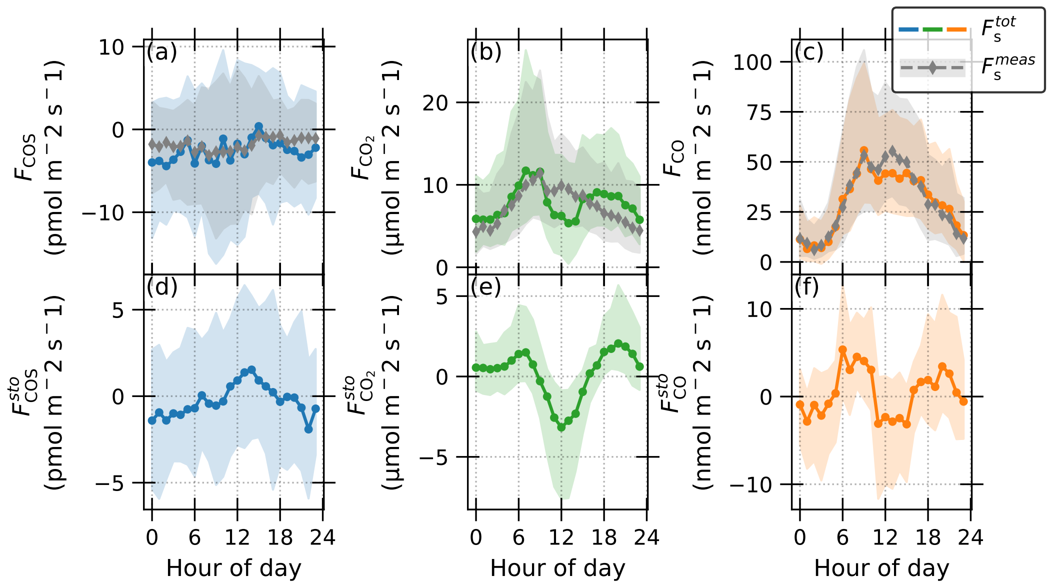

Figure A3. Measured and storage corrected of (a) COS, (b) CO_2, and (c) CO, as well as the storage fluxes of (d) COS, (e) CO_2, and (f) CO. Markers show the hourly medians and the coloured areas indicate the interquartile ranges.

https://doi.org/10.5194/egusphere-2026-4603
Preprint. Discussion started: 24 August 2026

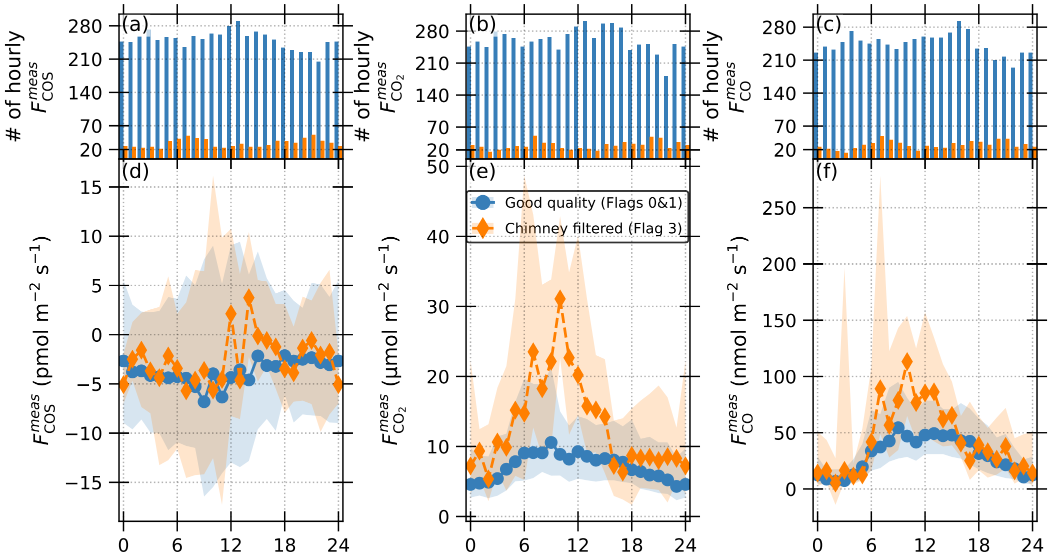

Figure A4. Diurnal fluxes with (orange) and without the emissions (blue) of the close-by chimney. Top panels (a), (b), (e), (f) show the hourly available data and bottom panels (c), (d), (g), and (h) show the diurnal fluxes of COS, CO_2, CO, and CH_4, respectively. Medians are shown with markers and lines, with the interquartile range as the shaded area. Shown fluxes are not storage corrected.

https://doi.org/10.5194/egusphere-2026-4603
Preprint. Discussion started: 24 August 2026

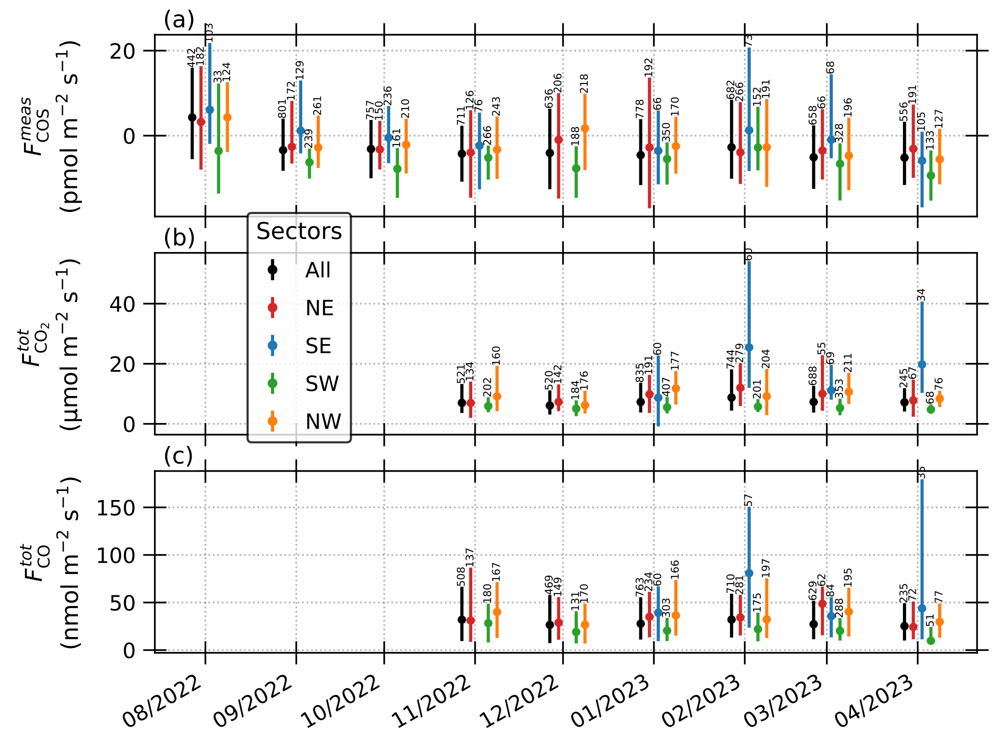

Figure A5. Monthly medians of (a) F_{COS}^{meas}, (b) $F_{\mathrm{CO_2}}^{tot}$, and (c) F_{CO}^{tot} in the full footprint and in each sector. Error bars indicate the monthly median and the interquartile range. Values are derived as temporally weighted quantiles to reduce biases associated with uneven sampling of wind directions across the diurnal and seasonal cycles. Number of monthly available data is shown above each error bar. Sector was only included if it had at least 30 data points for the month.

https://doi.org/10.5194/egusphere-2026-4603
Preprint. Discussion started: 24 August 2026

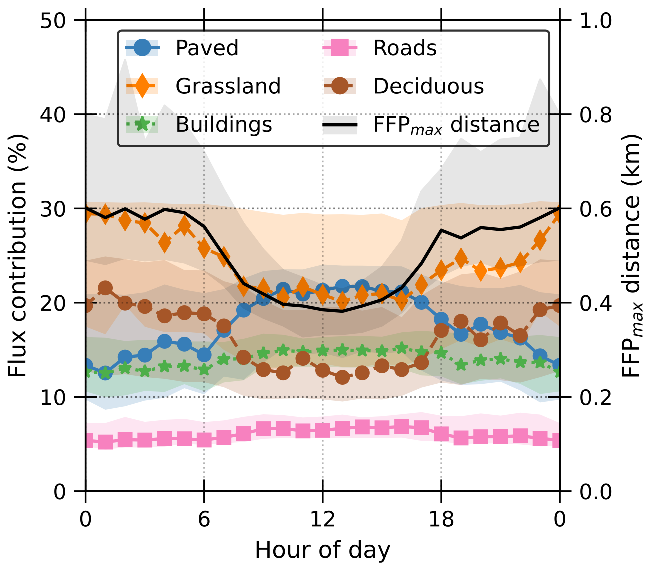

Figure A6. Diurnal cycles of the five land covers with the largest importance to observed fluxes according to the FFP model, and the distance of the FFP maximum value from the Hardau II tower (secondary axes). The hourly median and the interquartile range are shown for each land cover.

https://doi.org/10.5194/egusphere-2026-4603
Preprint. Discussion started: 24 August 2026

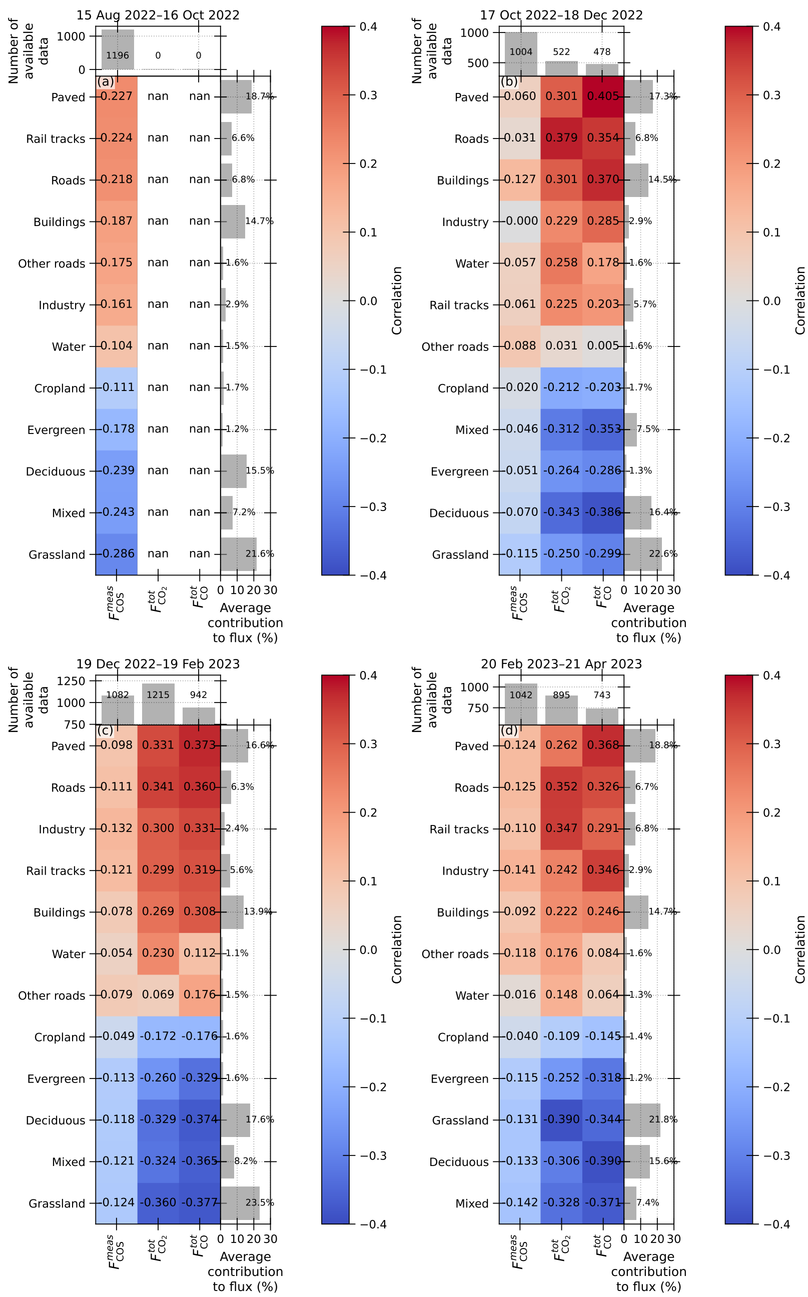

Figure A7. Same as Fig. 5, but for four sub-periods of the measurement period: 15 August – 16 October 2022, 17 October – 18 December 2022, 19 December 2022 – 19 February 2023, and 20 February – 21 April 2023.

https://doi.org/10.5194/egusphere-2026-4603
Preprint. Discussion started: 24 August 2026

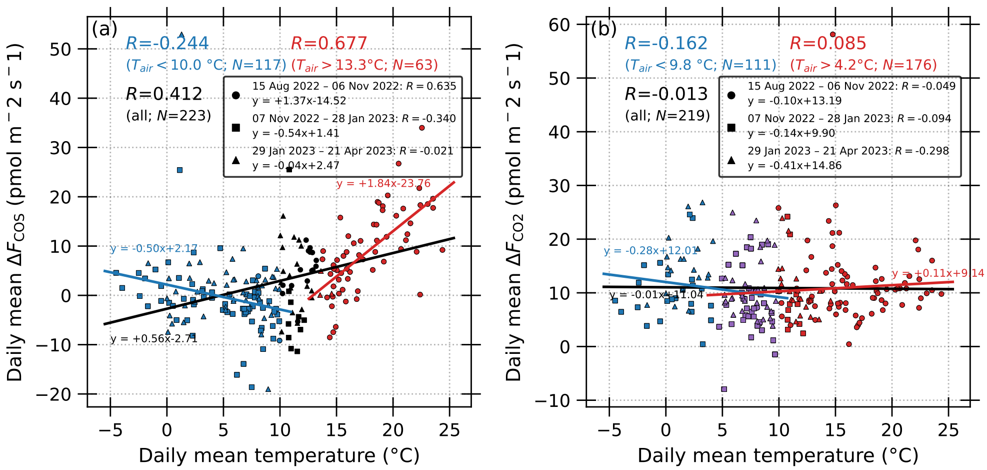

Figure A8. Temperature dependence of the daily mean difference between observed (F_s^{meas}) and SiB4 modelled (F_s^{SiB4}) fluxes of (a) COS and (b) CO_2. The difference is indicated with bars: Positive (blue) and negative (red) bars indicate that the model has assumed higher or lower sinks of COS compared to measurements, respectively. The black line shows the daily mean temperature.

https://doi.org/10.5194/egusphere-2026-4603
Preprint. Discussion started: 24 August 2026

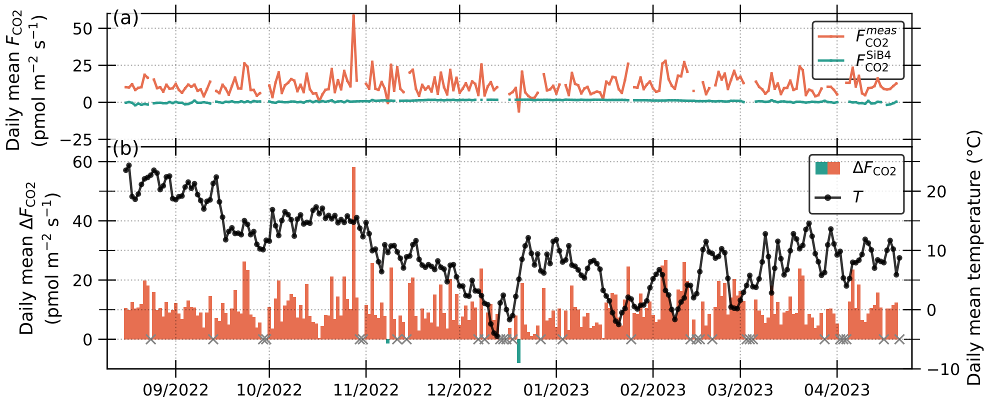

Figure A9. Same as Fig. 6, but for CO_2

https://doi.org/10.5194/egusphere-2026-4603
Preprint. Discussion started: 24 August 2026

Table A1. Monthly statistics of selected environmental variables. The key numbers are calculated as monthly arithmetic means for all variables except for precipitation, which is shown as the monthly sum. $\overline{T}_{air}$ denotes the long-term (2000–2020) air temperature on each month

Month	$\overline{T}_{air}$ (°C)	T_{air} (°C)	Precipitation (mm)	VPD (kPa)	SWC (m^3 m^{-3})
August 2022	20.8	22.6	69.3	1.25	0.23
September 2022	16.6	16.2	111.0	0.58	0.27
October 2022	12.1	15.1	73.4	0.32	0.31
November 2022	7.0	8.8	78.0	0.20	0.33
December 2022	3.5	4.0	91.0	0.13	0.34
January 2023	2.7	4.3	49.8	0.20	0.34
February 2023	3.4	4.8	19.2	0.26	0.33
March 2023	7.4	8.4	95.2	0.41	0.33
April 2023	11.8	9.8	93.8	0.40	0.33
Full period	8.7	9.6	632.3	0.35	0.32

https://doi.org/10.5194/egusphere-2026-4603
Preprint. Discussion started: 24 August 2026

Table A2. Monthly median values and interquartile ranges (25th–75th percentiles) of COS, CO_2, and CO fluxes from August 2022 to April 2023. Values are reported as median an interquartile range (Q25–Q75). Values both with (F_s^{tot}) and without (F_s^{meas}) storage correction are reported for each gas. Data flagged with quality flag 0 were used to calculate the values.

Month	F_{COS}^{meas} (pmol m^{-2} s^{-1})	F_{COS}^{tot}	$F_{CO_2}^{meas}$ (µmol m^{-2} s^{-1})	$F_{CO_2}^{tot}$	F_{CO}^{meas} (nmol m^{-2} s^{-1})	F_{CO}^{tot}
Aug 2022	4.6 (-4.7 – 15.5)	–	7.7 (4.0 – 14.0)	–	33.8 (15.7 – 73.9)	–
Sep 2022	-4.2 (-8.6 – 3.1)	–	5.5 (3.3 – 10.2)	–	27.4 (8.5 – 56.8)	–
Oct 2022	-3.8 (-9.9 – 3.3)	–	7.2 (4.0 – 13.7)	–	30.3 (11.7 – 70.5)	–
Nov 2022	-4.5 (-10.2 – 0.6)	-4.4 (-9.3 – 1.4)	7.5 (4.8 – 13.7)	7.3 (4.1 – 12.3)	34.7 (13.9 – 73.1)	32.1 (11.8 – 68.7)
Dec 2022	-4.6 (-12.6 – 5.1)	-3.7 (-14.1 – 4.4)	6.7 (4.3 – 11.3)	5.9 (3.1 – 11.1)	28.1 (11.2 – 54.1)	26.1 (6.9 – 52.8)
Jan 2023	-5.3 (-11.9 – 2.4)	-4.6 (-12.4 – 3.8)	7.5 (4.9 – 14.0)	7.3 (3.9 – 14.0)	28.9 (13.7 – 55.8)	28.2 (11.1 – 55.8)
Feb 2023	-3.6 (-10.2 – 7.7)	-3.3 (-13.5 – 9.4)	9.1 (5.3 – 16.4)	8.6 (4.4 – 17.3)	34.0 (14.8 – 56.5)	31.9 (13.2 – 54.2)
Mar 2023	-5.6 (-13.5 – -0.0)	-4.7 (-15.0 – 4.9)	6.9 (4.7 – 11.0)	6.9 (3.7 – 11.6)	23.7 (11.3 – 49.2)	24.9 (9.4 – 50.6)
Apr 2023	-5.9 (-11.9 – 3.3)	-6.4 (-13.1 – 0.2)	7.6 (5.0 – 12.5)	7.6 (4.6 – 11.0)	26.5 (13.3 – 50.3)	23.8 (9.7 – 42.4)
All data	-4.4 (-10.8 – 3.9)	-4.4 (-13.0 – 4.4)	7.1 (4.3 – 12.8)	7.2 (3.9 – 13.4)	29.2 (12.5 – 58.0)	28.0 (10.5 – 54.3)

https://doi.org/10.5194/egusphere-2026-4603
Preprint. Discussion started: 24 August 2026

Table A3. Flux contribution (%) from different land cover classes based on the FFP footprint. Values in parentheses indicate the corresponding land cover area fractions (%) within a 2.9 km radius of the Hardau II tower. The three lowermost rows show the summed contributions of vegetated (grassland, cropland, deciduous, evergreen, and mixed forests), impervious (paved surfaces, roads, rail tracks, and other roads), and built (buildings and industry) land cover classes. The sector 60–120° was excluded due to the orientation of the eddy covariance (EC) setup.

Wind dir.	Full footprint (0–360°)	NE (0–60°)	SE (120–200°)	SW (200–260°)	NW (260–360°)
Grassland	22.4 (22.0)	14.4 (20.0)	18.8 (23.0)	30.2 (29.5)	21.6 (25.4)
Paved	17.9 (16.7)	21.6 (14.2)	18.2 (17.8)	11.6 (8.6)	23.6 (18.9)
Deciduous	16.3 (17.0)	10.8 (22.1)	14.3 (14.1)	22.8 (29.7)	13.0 (12.9)
Buildings	14.4 (17.7)	15.9 (14.6)	19.9 (21.9)	11.9 (10.5)	14.3 (14.7)
Mixed	7.6 (7.6)	4.1 (8.0)	7.7 (7.8)	11.0 (12.1)	6.2 (5.3)
Roads	6.6 (7.8)	7.8 (7.1)	9.0 (9.2)	5.0 (4.6)	6.7 (7.5)
Rail tracks	6.2 (4.1)	15.2 (4.1)	1.2 (1.3)	0.4 (0.4)	5.6 (6.3)
Industry	2.8 (1.7)	4.4 (2.1)	1.2 (1.5)	1.1 (0.5)	4.3 (3.2)
Cropland	1.6 (1.1)	1.1 (2.2)	0.6 (0.1)	2.2 (0.5)	1.7 (2.2)
Other roads	1.6 (1.6)	2.6 (1.8)	1.6 (1.5)	1.3 (0.9)	0.8 (1.3)
Evergreen	1.3 (0.9)	0.5 (1.9)	0.6 (0.2)	2.2 (2.6)	1.3 (0.5)
Water	1.4 (1.9)	1.5 (1.8)	7.0 (1.6)	0.3 (0.1)	0.7 (1.8)
Vegetation	49.1 (48.6)	31.0 (54.2)	41.9 (45.2)	68.5 (74.4)	43.9 (46.3)
Impervious	32.3 (30.2)	47.2 (27.2)	30.0 (29.8)	18.3 (14.5)	36.8 (34.0)
Built	17.2 (19.4)	20.3 (16.7)	21.1 (23.4)	13.0 (11.0)	18.7 (17.9)

Code availability. The codes used for the data analysis will be made available in the Zenodo repository under the Creative Commons Licence CCBY-4.0 (https://doi.org/10.5281/zenodo.21626128).

Data availability. EC flux time series archive (L2) from Hardau were downloaded from the ICOS Carbon portal, DOI: https://doi.org/10.18160/G039-HZT1 (Soininen et al., 2025b). FFP footprint functions were downloaded from the ICOS Carbon portal, DOI (Molinier and Kljun, 2026). The FFP footprint model is freely available at footprint.kljun.net. The used meteorological data are available in the Zenodo repository under the Creative Commons Licence CCBY-4.0, DOI: https://doi.org/10.5194/bg-22-2133-2025 (Stagakis et al., 2024). The global data set of anthropogenic COS emissions is openly available by Campbell Lab Data Share (Zumkehr et al., 2018b). Kaserne station data have been downloaded from https://www.bafu.admin.ch/en/data-query-nabel. SiB4 model results are included and openly available in the Zenodo repository under the Creative Commons Licence CCBY-4.0 (https://doi.org/10.5281/zenodo.21626128).

https://doi.org/10.5194/egusphere-2026-4603
Preprint. Discussion started: 24 August 2026

Author contributions. Conceptualization: JS, K-MK, LJ. Methodology: JS, K-MK, SS, AC, BM, RH, NK, LJ. Formal analysis: JS, SS, AC, BM, RH. Investigation: JS, K-MK, LJ. Data curation: JS, SS, AC, BM. Writing (original draft): JS, K-MK, LJ. Writing (review & editing): All. Visualization: JS. Supervision: K-MK, NK, LJ. Funding acquisition: SS, NK, LJ. Project administration: LJ.

Competing interests. The authors declare that they have no conflict of interest.

Acknowledgements. This work is supported by the PAUL (Pilot Applications in Urban Landscapes - Towards integrated city observatories for greenhouse gases; ICOS Cities), which has received funding from the European Union's Horizon 2020 Research and Innovation Programme under grant agreement No. 101037319, the University of Helsinki through a university-funded doctoral researcher position, and the Research Council of Finland Flagship ACCC (357902 and 359340). Financial support from ICOS Switzerland (ICOS-CH) Phase 3 and Phase 4 (Swiss National Science Foundation, grants 20FI20_198227, 20FI-0_229655) is also acknowledged.

https://doi.org/10.5194/egusphere-2026-4603
Preprint. Discussion started: 24 August 2026

References

Asaf, D., Rotenberg, E., Tatarinov, F., Dicken, U., Montzka, S. A., and Yakir, D.: Ecosystem photosynthesis inferred from measurements of carbonyl sulphide flux, Nat. Geosci., 6, 186–190, https://doi.org/10.1038/NGEO1730, 2013.

Aubinet, M., Vesala, T., and Papale, D., (Eds.): Eddy Covariance - A practical guide to measurement and data analysis, Springer Science, https://doi.org/10.1007/978-94-007-2351-1, 2012.

Auvinen, M., Järvi, L., Hellsten, A., Rannik, Ü., and Vesala, T.: Numerical framework for the computation of urban flux footprints employing large-eddy simulation and Lagrangian stochastic modeling, Geosci. Model. Dev, 10, 4187–4205, https://doi.org/10.5194/gmd-10-4187-2017, 2017.

Baartman, S. L., Krol, M. C., Röckmann, T., Hattori, S., Kamezaki, K., Yoshida, N., and Popa, M. E.: A GC-IRMS method for measuring sulfur isotope ratios of carbonyl sulfide from small air samples, Open Res. Europe, 1, 105, https://doi.org/10.12688/openreseurope.13875.2, 2022.

Berry, J., Wolf, A., Campbell, J. E., Baker, I., Blake, N., Blake, D., Denning, A. S., Kawa, S. R., Montzka, S. A., Seibt, U., Stimler, K., Yakir, D., and Zhu, Z: A coupled model of the global cycles of carbonyl sulfide and CO_2: A possible new window on the carbon cycle, J. Geophys. Res., Biogeosciences, 118, 842–852, https://doi.org/10.1002/jgrg.20068, 2013.

Belviso, S., Pison, I., Petit, J.-E., Berchet, A., Remaud, M., Simon, L., Ramonet, M., Delmotte, M., Kazan, V., Yver-Kwok, C., and Lopez, M.: The Z-2018 emissions inventory of COS in Europe: A semiquantitative multi-data-streams evaluation, Atmos. Environ., 300, 119 689, https://doi.org/10.1016/j.atmosenv.2023.119689, 2023.

Blonquist, J. M. J., Montzka, S. A., Munger, J. W., Yakir, D., Desai, A. R., Dragoni, D., Griffis, T. J., Monson, R. K., Scott, R. L., and Bowling, D. R.: The potential of carbonyl sulfide as a proxy for gross primary production at flux tower sites, J. Geophys. Res., 116, G04 019, https://doi.org/10.1029/2011JG001723, 2011.

Cheng, Y., Zhang, C., Zhang, Y., Zhang, H., Sun, X., and Mu, Y.: Characteristics and anthropogenic sources of carbonyl sulfide in Beijing, J. Environ. Sci., 28, 163–170, https://doi.org/10.1016/J.JES.2014.05.052, 2015.

Cho, A., Kooijmans, L. M. J., Kohonen, K.-M., Wehr, R., and Krol, M. C.: Optimizing the carbonic anhydrase temperature response and stomatal conductance of carbonyl sulfide leaf uptake in the Simple Biosphere model (SiB4), Biogeosciences, 20, 2573–2594, https://doi.org/10.5194/bg-20-2573-2023, 2023.

Cho, A., Kooijmans, L. M. J., Driever, S.M., Wassenaar, M., Koren, G.,. Baartman, S. L., Mossink, L., and Krol, M. C.: Leaf chamber experiments on sunflowers indicate a temperature-dependent compensation point of carbonyl sulfide [version 3; peer review: 2 approved, 1 approved with reservations], Open Res. Europe, 5, 223, https://doi.org/10.12688/openreseurope.20235.3, 2026.

Commane, R., Meredith, L. K., Baker, I. T., Berry, J. A., Munger, J. W., Montzka, S. A., Templer, P. H., Juice, S. M., Zahniser, M. S., and Wofsy, S. C.: Seasonal fluxes of carbonyl sulfide in a midlatitude forest, P. Natl. Acad. Sci. USA, 112, 14 162–14 167, https://doi.org/10.1073/pnas.1504131112, 2015.

Crawford, B. and Christen, A.: Spatial source attribution of measured urban eddy covariance CO_2 fluxes, Theor. Appl. Climatol., 119, 733–755, https://doi.org/10.1007/s00704-014-1124-0, 2015.

Estruch, C., Belviso, S., Badia, A., Vidal, V., Curcoll, R., Udina, M., Grossi, C., Morguí, J.-A., Segura, R., Ventura, S., Sola, Y., and Villalba, G.: Exploring the Influence of Land Use on the Urban Carbonyl Sulfide Budget: A Case Study of the Metropolitan Area of Barcelona, J. Geophys. Res.: Atmospheres, 128, e2023JD039 497, https://doi.org/10.1029/2023JD039497, 2023.

https://doi.org/10.5194/egusphere-2026-4603
Preprint. Discussion started: 24 August 2026

Finnigan, J.: The storage term in eddy flux calculations, Agr. Forest. Meteorol., 136, 108–113, https://doi.org/10.1016/j.agrformet.2004.12.010, 2006.

Foken, T. and Wichura, B.: Tools for quality assessment of surface-based flux measurements, Agr. Forest. Meteorol., 78, 83–105, https://doi.org/10.1016/0168-1923(95)02248-1, 1996.

Garvey, S. M., Templer, P. H., Pierce, E. A., Reinmann, A. B., and Hutyra, L. R.: Diverging patterns at the forest edge: Soil respiration dynamics of fragmented forests in urban and rural areas, Glob. Change Biol., 28, 3094–3109. https://doi.org/10.1111/gcb.16099, 2022.

Gelaro, R., McCarty, W., Suárez, M. J., Todling, R., Molod, A., Takacs, L., Randles, C. A., Darmenov, A., Bosilovich, M. G., Reichle, R., Wargan, K., Coy, L., Cullather, R., Draper, C., Akella, S., Buchard, V., Conaty, A., da Silva, A. M., Gu, W., Kim, G., Koster, R., Lucchesi, R., Merkova, D., Nielsen, J. E., Partyka, G., Pawson, S., Putman, W., Rienecker, M., Schubert, S. D., Sienkiewicz, M., and Zhao, B.: The modern-era retrospective analysis for research and applications, version 2 (MERRA-2), J. Climate, 30, 5419–5454, https://doi.org/10.1175/JCLI-D-16-0758.1, 2017.

Gerdel, K., Spielmann, F. M., Hammerle, A., and Wohlfahrt, G.: Eddy covariance carbonyl sulfide flux measurements with a quantum cascade laser absorption spectrometer, Atmos. Meas. Tech., 10, 3525–3537, https://doi.org/10.5194/amt-10-3525-2017, 2017.

Gurney, K.R., Kılkış, Ş., Seto, K.C., Lwasa, S., Moran, D., Riahi, K., Keller, M., Rayner, P. and Luqman, M.: Greenhouse Gas Emissions from Global Cities under SSP/RCP Scenarios, 1990 to 2100, Global Environmental Change, 73, 102478, https://doi.org/10.1016/j.gloenvcha.2022.102478, 2022.

Haynes, K. D., Baker, I.T., Denning, A.S., Stöckli, R., Schaefer, K., Lokupitiya, E.Y., and Haynes, J. M.: Representing Grasslands Using Dynamic Prognostic Phenology Based on Biological Growth Stages: 1. Implementation in the Simple Biosphere Model (SiB4), J. Adv. Model. Earh. Sy., 11, 4423–4439, https://doi.org/10.1029/2018MS001540, 2019.

Helfter, C., Tremper, A. H., Halios, C. H., Kotthaus, S., Bjorkegren, A., Grimmond, C. S. B., Barlow, J. F., and Nemitz, E.: Spatial and temporal variability of urban fluxes of methane, carbon monoxide and carbon dioxide above London, UK, Atmos. Chem. Phys., 16, 10 543–10 557, https://doi.org/10.5194/acp-16-10543-2016, 2016.

Hilland, R., Hashemi, J., Stagakis, S., Brunner, D., Constantin, L., Kljun, N., Kunz, A.-K., Molinier, B., Hammer, S., Emmenegger, L., and Christen, A.: Sectoral attribution of greenhouse gas and pollutant emissions using multi-species eddy covariance on a tall tower in Zurich, Switzerland, Atmos. Chem. Phys., 25, 14 279–14 299, https://doi.org/10.5194/acp-25-14279-2025, 2025.

Hüglin, C., Buchmann, B., Steinbacher, M., and Emmenegger, L.: The swiss national air pollution monitoring network (NABEL) – bridging science and environmental policy, Chimia, 78, 722–727, https://doi.org/10.2533/chimia.2024.722, 2024.

ICOS: ICOS Cities, https://www.icos-cp.eu/projects/icos-cities, last access: 29 July 2026.

IEA: Austria 2020 - Energy Policy Review, International Energy Agency, Paris, https://www.iea.org/reports/austria-2020, 2020.

Jasek-Kamińska, A., Zimnoch, M., Wachniew, P., and Różański, K.: Urban CO_2 Budget: Spatial and Seasonal Variability of CO_2 Emissions in Krakow, Poland, Atmosphere, 11, 629, https://doi.org/10.3390/atmos11060629, 2020.

Jocher, G., Marshall, J., Nilsson, M. B., Linder, S., De Simon, G., Hörnlund, T., Lundmark, T., Näsholm, T., Ottosson Löfvenius, M., Tarvainen, L., Wallin, G., and Peichl, M.: Impact of Canopy Decoupling and Subcanopy Advection on the Annual Carbon Balance of a Boreal Scots Pine Forest as Derived From Eddy Covariance, J. Geophys. Res.: Biogeosciences, 123, 303–325. https://doi.org/10.1002/2017JG003988, 2018.

Järvi, L., Nordbo, A., Junninen, H., Riikonen, A., Moilanen, J., Nikinmaa, E., and Vesala, T.: Seasonal and annual variation of carbon dioxide surface fluxes in Helsinki, Finland, in 2006–2010, Atmos. Chem. Phys., 12, 8475–8489, https://doi.org/10.5194/acp-12-8475-2012, 2012.

Kanton Zürich: Amtliche Vermessung; Bodenbedeckung DM01AVZH24 [data set], http://geolion.zh.ch/api/v2/getGeodatenmeta.html?giszhnr=443, Last accessed 24.11.2025, 2017.

Karl, T., Gohm, A., Rotach, M. W., Ward, H. C., Graus, M., Cede, A., Wohlfahrt, G., Hammerle, A., Haid, M., Tiefengraber, M., Lamprecht, C., Vergeiner, J., Kreuter, A., Wagner, J., and Staudinger, M.: Studying urban climate and air quality in the Alps, B. Am. Meteorol. Soc., 101, E488–E507, https://doi.org/10.1175/BAMS-D-19-0270.1, 2020.

Kauffman, G. B.: Eduard Schweizer (1818-1860): The unknown chemist and his well-known reagent, J. Chem. Educ., 61, 1095, https://doi.org/10.1021/ed061p1095, 1984.

Kleingeld, E., van Hove, B., Elbers, J., and Jacobs, C.: Carbon dioxide fluxes in the city centre of Arnhem, A middle-sized Dutch city, Urban Climate, 24, 994–1010, https://doi.org/10.1016/J.UCLIM.2017.12.003, 2018.

Kljun, N., Calanca, P., Rotach, M. W., and Schmid, H. P.: A simple two-dimensional parameterisation for Flux Footprint Prediction (FFP), Geosci. Model. Dev, 8, 3695–3713, https://doi.org/10.5194/gmd-8-3695-2015, 2015.

Kohonen, K. M., Kolari, P., Kooijmans, L. M., Chen, H., Seibt, U., Sun, W., and Mammarella, I.: Towards standardized processing of eddy covariance flux measurements of carbonyl sulfide, Atmos. Meas. Tech., 13, 3957–3975, https://doi.org/10.5194/amt-13-3957-2020, 2020.

Kohonen, K.-M., Dewar, R., Tramontana, G., Mauranen, A., Kolari, P., Kooijmans, L. M. J., Papale, D., Vesala, T., and Mammarella, I.: Intercomparison of methods to estimate gross primary production based on CO2 and COS flux measurements, Biogeosciences, 19, 4067–4088, https://doi.org/10.5194/bg-19-4067-2022, 2022.

Kooijmans, L. M., Sun, W., Aalto, J., Erkkilä, K. M., Maseyk, K., Seibt, U., Vesala, T., Mammarella, I., and Chen, H.: Influences of light and humidity on carbonyl sulfide-based estimates of photosynthesis, P. Natl. Acad. Sci. USA, 116, 2470–2475, https://doi.org/10.1073/pnas.1807600116, 2019.

Kooijmans, L. M. J., Maseyk, K., Seibt, U., Sun, W., Vesala, T., Mammarella, I., Kolari, P., Aalto, J., Franchin, A., Vecchi, R., Valli, G., and Chen, H.: Canopy uptake dominates nighttime carbonyl sulfide fluxes in a boreal forest, Atmos. Chem. Phys., 17, 11 453–11 465, https://doi.org/10.5194/acp-17-11453-2017, 2017.

Kooijmans, L. M. J., Cho, A., Ma, J., Kaushik, A., Haynes, K. D., Baker, I., Luijkx, I. T., Groenink, M., Peters, W., Miller, J. B., Berry, J. A., Ogée, J., Meredith, L. K., Sun, W., Kohonen, K.-M., Vesala, T., Mammarella, I., Chen, H., Spielmann, F. M., Wohlfahrt, G., Berkelhammer, M., Whelan, M. E., Maseyk, K., Seibt, U., Commane, R., Wehr, R., and Krol, M.: Evaluation of carbonyl sulfide biosphere exchange in the Simple Biosphere Model (SiB4), Biogeosciences, 18, 6547–6565, https://doi.org/10.5194/bg-18-6547-2021, 2021.

Lan, C., Holst, C. C., Grünwald, T., and Mauder, M.: Linkage Between Vertical Coupling and Storage Flux: Insights from Urban Tall-Tower Eddy Covariance Measurement, Bound.-Lay. Meteorol., 191, 4, https://doi.org/10.1007/s10546-024-00894-6, 2025.

Lee, K., Hong, J. W., Kim, J., and Hong, J.: Partitioning of net CO_2 exchanges at the city-atmosphere interface into biotic and abiotic components, MethodsX, 8, https://doi.org/10.1016/J.MEX.2021.101231, 2021.

Li, J., Chen, J., Glauch, T., Brunner, D., Marshall, J., Ponomarev, N., Tang, H., and Stagakis, S.: Fine-scale estimation of urban biogenic CO2 fluxes: A novel framework integrating multiple versions of vegetation photosynthesis and respiration models and in situ measurements, Earth's Future, 14, e2025EF007458, https://doi.org/10.1029/2025EF007458, 2026.

Mahrt, L., Sun, J., Blumen, W., Delany, T., and Oncley, S.: Nocturnal boundary-layer regimes, Bound.-Lay. Meteorol., 88, 255–278, https://doi.org/10.1023/A:1001171313493/METRICS, 1998.

Mammarella, I., Launiainen, S., Gronholm, T., Keronen, P., Pumpanen, J., Rannik, Ü., and Vesala, T.: Relative Humidity Effect on the High-Frequency Attenuation of Water Vapor Flux Measured by a Closed-Path Eddy Covariance System, J. Atmos. Ocean. Tech., 26, 1856–1866, https://doi.org/10.1175/2009JTECHA1179.1, 2009.

Maseyk, K., Berry, J. A., Billesbach, D., Campbell, J. E., Torn, M. S., Zahniser, M., and Seibt, U.: Sources and sinks of carbonyl sulfide in an agricultural field in the Southern Great Plains, P. Natl. Acad. Sci. USA, 111, 9064–9069, https://doi.org/10.1073/PNAS.1319132111/-/DCSUPPLEMENTAL/PNAS.201319132SI.PDF, 2014.

Matese, A., Gioli, B., Vaccari, F. P., Zaldei, A., and Miglietta, F.: Carbon dioxide emissions of the city center of Firenze, Italy: Measurement, evaluation, and source partitioning, J. Appl. Meteorol. Clim., 48, 1940–1947, https://doi.org/10.1175/2009JAMC1945.1, 2009.

Menzer, O. and McFadden, J. P.: Statistical partitioning of a three-year time series of direct urban net CO_2 flux measurements into biogenic and anthropogenic components, Atmos. Environ., 170, 319–333, https://doi.org/10.1016/j.atmosenv.2017.09.049, 2017.

Molinier, B. and Kljun, N.: Zurich-Hardau flux footprints, ICOS RI [data set], https://doi.org/10.18160/G26R-E8P3, 2026.

Molinier, B., Aigner, P., Brunner, D., Chen, J., Christen, A., Constantin, L., Denier van der Gon, H., Hilland, R., Kühbacher, D., Li, J., Maiwald, R., Super, I., Vardag, S. N., and Kljun, N.: Insights from the Convolution of Emission Inventories with Flux Footprints from Tall Eddy Covariance Towers at Three European Cities, ACS ES&T Air, 3, 1664–1676. https://doi.org/10.1021/acsestair.6c00148, 2026.

Montagnani, L., Grünwald, T., Kowalski, A., Mammarella, I., Merbold, L., Metzger, S., Sedlák, P., and Siebicke, L.: Estimating the storage term in eddy covariance measurements: The ICOS methodology, Int. Agrophys., 32, 551–567, https://doi.org/10.1515/intag-2017-0037, 2018.

Montzka, S. A., Calvert, P., Hall, B. D., Elkins, J. W., Conway, T. J., Tans, P. P., and Sweeney, C. S.: On the global distribution, seasonality, and budget of atmospheric carbonyl sulfide (COS) and some similarities to CO_2, J. Geophys. Res.: Atmospheres, 112, D09 302, https://doi.org/10.1029/2006JD007665, 2007.

Moreau, J.-P.: Suisse : Le réseau ferroviaire fédéral entièrement électrifié, Ann. Geogr., 375, 544–545, https://www.persee.fr/doc/geo_0003-4010_1960_num_69_375_14750, 1960.

Ogée, J., Sauze, J., Kesselmeier, J., Genty, B., Van Diest, H., Launois, T., and Wingate, L.: A new mechanistic framework to predict OCS fluxes from soils, Biogeosciences 13, 2221–2240, https://doi.org/10.5194/bg-13-2221-2016, 2016.

Peters, E. B. and McFadden, J. P.: Continuous measurements of net CO_2 exchange by vegetation and soils in a suburban landscape, J. Geophys. Res.: Biogeosciences, 117, https://doi.org/10.1029/2011JG001933, 2012.

Pos, W. H. and Berresheim, H.: Automotive tire wear as a source for atmospheric OCS and CS2, Geophys. Res. Lett., 20, 815–817, https://doi.org/10.1029/93GL00972, 1993.

Sabbatini, S., Mammarella, I., Arriga, N., Fratini, G., Graf, A., Hörtnagl, L., Ibrom, A., Longdoz, B., Mauder, M., Merbold, L., Metzger, S., Montagnani, L., Pitacco, A., Rebmann, C., Sedlák, P., Šigut, L., Vitale, D., and Papale, D.: Eddy covariance raw data processing for CO_2 and energy fluxes calculation at ICOS ecosystem stations, Int. Agrophys., 32, 495–515, https://doi.org/10.1515/intag-2017-0043, 2018.

Salgueiro, V., Cerqueira, M., Monteiro, A., Alves, C., Rafael, S., Borrego, C., and Pio, C.: Annual and seasonal variability of greenhouse gases fluxes over coastal urban and suburban areas in Portugal: Measurements and source partitioning, Atmos. Environ., 223, https://doi.org/10.1016/J.ATMOSENV.2019.117204, 2020.

Scapucci, L., Shekhar, A., Aranda-Barranco, S., Bolshakova, A., Hörtnagl, L., Gharun, M., and Buchmann, N.: Compound soil and atmospheric drought (CSAD) events and CO_2 fluxes of a mixed deciduous forest: the occurrence, impact, and temporal contribution of main drivers, Biogeosciences, 21, 3571–3592, https://doi.org/10.5194/bg-21-3571-2024, 2024.

Soininen, J., Kohonen, K.-M., Rantala, P., Kulmala, L., Aaltonen, H., and Järvi, L.: Carbon uptake of an urban green space inferred from carbonyl sulfide fluxes, npj Climate and Atmospheric Science, 8, 90, https://doi.org/10.1038/s41612-025-00958-5, 2025a.

Soininen, J., Brunner, D., Emmenegger, L., Rubli, P., Stagakis, S., and Järvi, L.: EC flux time series archive (L2), Hardau, 2022-08-15–2023-04-21, ICOS RI [data set], https://doi.org/10.18160/G039-HZT1, 2025b.

https://doi.org/10.5194/egusphere-2026-4603
Preprint. Discussion started: 24 August 2026

Song, T., Wang, Y., and Sun, Y.: Estimation of carbon dioxide flux and source partitioning over Beijing, China, J. Environ. Sci., 25, 2429–2434, https://doi.org/10.1016/S1001-0742(12)60336-2, 2013.

Spielmann, F. M., Hammerle, A., Kitz, F., Gerdel, K., and Wohlfahrt, G.: Seasonal dynamics of the COS and CO_2 exchange of a managed temperate grassland, Biogeosciences, 17, 4281–4295, https://doi.org/10.5194/bg-17-4281-2020, 2020.

Spielmann, F. M., Kitz, F., Roach, T., Kranner, I., Hammerle, A., and Wohlfahrt, G.: Effects of drought on carbonyl sulfide exchange in four plant species, Plant Stress, 15, 100 735, https://doi.org/10.1016/j.stress.2024.100735, 2025.

Squires, F. A., Nemitz, E., Langford, B., Wild, O., Drysdale, W. S., Acton, W. J. F., Fu, P., Grimmond, C. S. B., Hamilton, J. F., Hewitt, C. N., Hollaway, M., Kotthaus, S., Lee, J., Metzger, S., Pingintha-Durden, N., Shaw, M., Vaughan, A. R., Wang, X., Wu, R., Zhang, Q., and Zhang, Y.: Measurements of traffic-dominated pollutant emissions in a Chinese megacity, Atmos. Chem. Phys., 20, 8737–8761, https://doi.org/10.5194/acp-20-8737-2020, 2020.

Stadt Zürich: Net Zero Progress Report 2024, https://www.stadt-zuerich.ch/content/dam/web/de/aktuell/publikationen/2024/klimaschutz/net-zero-progress-report-2024.pdf, Last accessed 12 December 2025, 2024.

Stadt Zürich: Primärenergieverbrauch, https://www.stadt-zuerich.ch/content/dam/web/de/politik-verwaltung/statistik-und-daten/daten/umwelt-energie/UMW104JM1041_Primaerenergieverbrauch.xlsx, Last accessed 26 May 2026, 2025.

Stadt Zürich: Strom, Wärme und Gas, https://www.stadt-zuerich.ch/content/dam/web/de/politik-verwaltung/statistik-und-daten/daten/umwelt-energie/Strom_Waerme_und_Gas.xlsx, Last accessed 26 May 2026, 2025.

Stagakis, S., Chrysoulakis, N., Spyridakis, N., Feigenwinter, C., and Vogt, R.: Eddy Covariance measurements and source partitioning of CO_2 emissions in an urban environment: Application for Heraklion, Greece, Atmos. Environ., 201, 278–292, https://doi.org/10.1016/J.ATMOSENV.2019.01.009, 2019.

Stagakis, S., Feigenwinter, C., Vogt, R., Brunner, D., and Kalberer, M.: A High-Resolution Monitoring Approach of Urban CO_2 Fluxes. Part 2 – Surface Flux Optimisation Using Eddy Covariance Observations, Sci. Total. Environ., 903, 166035, https://doi.org/10.1016/j.scitotenv.2023.166035, 2023.

Stagakis, S., Brunner, D., Li, J., Backman, L., Karvonen, A., Constantin, L., Järvi, L., Havu, M., Chen, J., Emberger, S., and Kulmala, L.: Dataset for the preprint: "Intercomparison of biogenic CO_2 flux models in four urban parks in the city of Zurich" (0.1) [Data set]. Zenodo [data set], https://doi.org/10.5281/zenodo.13222637, 2024.

Stagakis, S., Brunner, D., Li, J., Backman, L., Karvonen, A., Constantin, L., Järvi, L., Havu, M., Chen, J., Emberger, S., and Kulmala, L.: Intercomparison of biogenic CO_2 flux models in four urban parks in the city of Zurich, Biogeosciences, 22, 2133–2161, https://doi.org/10.5194/bg-22-2133-2025, 2025.

Strassenverkehrsamt des Kantons Zürich: Neuzulassungen im Kanton Zürich nach Antriebsart 2002–2025, https://daten.statistik.zh.ch/ogd/daten/ressourcen/KTZH_00000742_00001894.xlsx, Last accessed 19 November 2025, 2025.

Sun, W., Maseyk, K., Lett, C., and Seibt, U.: Restricted internal diffusion weakens transpiration–photosynthesis coupling during heatwaves: Evidence from leaf carbonyl sulphide exchange, Plant. Cell Environ., 47, 1813–1833, https://doi.org/10.1111/pce.14840, 2023.

Thomas, A., Laasonen, A., Kohonen, K.-M., Aslan, T., Sun, W., Dukat, P., Salmon, Y., Dewar, R., Kolari, P., Maseyk, K., Vesala, T., and Mammarella, I.: Examining anomalous summer carbonyl sulfide emissions in a boreal forest after thinning, npj Climate and Atmospheric Science, 9, 1, https://doi.org/10.1038/s41612-025-01272-w, 2026.

Turnbull, J. C., Karion, A., Davis, K. J., Lauvaux, T., Miles, N. L., Richardson, S. J., Sweeney, C., McKain, K., Lehman, S. J., Gurney, K. R., Patarasuk, R., Liang, J., Shepson, P. B., Heimburger, A., Harvey, R., and Whetstone, J.: Synthesis of Urban CO_2 Emission

Estimates from Multiple Methods from the Indianapolis Flux Project (INFLUX), Environmental Science & Technology, 53, 287–295, https://doi.org/10.1021/acs.est.8b05552, 2019.

United Nations: World Urbanization Prospects 2025: Summary of Results, UN DESA/POP/2025/TR/ NO. 12, United Nations, New York, https://www.un.org/development/desa/pd/sites/www.un.org.development.desa.pd/files/undesa_pd_2025_wup2025_summary_of_results.pdf, Last accessed 4 December 2025, 2025.

Vesala, T., Kohonen, K.-M., Kooijmans, L. M., Praplan, A. P., Foltýnová, L., Kolari, P., Kulmala, M., Bäck, J., Nelson, D., Yakir, D., Zahniser, M., and Mammarella, I.: Long-Term fluxes of carbonyl sulfide and their seasonality and interannual variability in a boreal forest, Atmos. Chem. Phys., 22, 2569–2584, https://doi.org/10.5194/acp-22-2569-2022, 2022.

Whelan, M. E., Lennartz, S. T., Gimeno, T. E., Wehr, R., Wohlfahrt, G., Wang, Y., Kooijmans, L. M. J., Hilton, T. W., Belviso, S., Peylin, P., Commane, R., Sun, W., Chen, H., Kuai, L., Mammarella, I., Maseyk, K., Berkelhammer, M., Li, K.-F., Yakir, D., Zumkehr, A., Katayama, Y., Ogée, J., Spielmann, F. M., Kitz, F., Rastogi, B., Kesselmeier, J., Marshall, J., Erkkilä, K.-M., Wingate, L., Meredith, L. K., He, W., Bunk, R., Launois, T., Vesala, T., Schmidt, J. A., Fichot, C. G., Seibt, U., Saleska, S., Saltzman, E. S., Montzka, S. A., Berry, J. A., and Campbell, J. E.: Reviews and syntheses: Carbonyl sulfide as a multi-scale tracer for carbon and water cycles, Biogeosciences, 15, 3625–3657, https://doi.org/10.5194/bg-15-3625-2018, 2018.

Wohlfahrt, G., Brilli, F., Hörtnagl, L., Xu, X., Bingemer, H., Hansel, A., and Loreto, F.: Carbonyl sulfide (COS) as a tracer for canopy photosynthesis transpiration and stomatal conductance: Potential and limitations, Plant. Cell Environ., 35, 657–667, https://doi.org/10.1111/J.1365-3040.2011.02451.X, 2012.

Wu, K., Davis, K. J., Miles, N. L., Richardson, S. J., Lauvaux, T., Sarmiento, D. P., Balashov, N. V., Keller, K., Turnbull, J., Gurney, K. R., Liang, J., and Roest, G.: Source decomposition of eddy-covariance CO_2 flux measurements for evaluating a high-resolution urban CO_2 emissions inventory, Environ. Res. Lett., 17, 074 035, https://doi.org/10.1088/1748-9326/ac7c29, 2022.

Zanchetta, A., Kooijmans, L. M. J., Van Heuven, S., Scifo, A., Scheeren, H. A., Mammarella, I., Karstens, U., Ma, J., Krol, M., and Chen, H.: Sources and sinks of carbonyl sulfide inferred from tower and mobile atmospheric observations in the Netherlands, Biogeosciences, 20, 3539–3553, https://doi.org/10.5194/bg-20-3539-2023, 2023.

Zumkehr, A., Hilton, T. W., Whelan, M., Smith, S., Kuai, L., Worden, J., and Campbell, J. E.: Global gridded anthropogenic emissions inventory of carbonyl sulfide, Atmos. Environ., 183, 11–19, https://doi.org/10.1016/j.atmosenv.2018.03.063, 2018a.

Zumkehr, A., Hilton, T. W., Whelan, M., Smith, S., Kuai, L., Worden, J., and Campbell, J. E.: Global gridded anthropogenic emissions inventory of carbonyl sulfide, Campbell Lab Data Sharing [data set], UC Santa Cruz, https://portal.nersc.gov/project/m2319/anthropogenic_OCS_AE/, Last accessed 11.12.2025, 2018b.